This is a preprint, the final version is subject to change, of the American Mineralogist (MSA)
Cite as Authors (Year) Title. American Mineralogist, in press.
(DOI will not work until issue is live.) DOI: http://dx.doi.org/10.2138/am-2016-5743

AM manuscript 5473- Revision 2

In situ elemental and isotopic analysis of fluorapatite from the Taocun magnetite-apatite deposit, Eastern China: Constraints on fluid metasomatism

Li-Ping Zeng[1], Xin-Fu Zhao[1,*], Xiao-Chun Li[2], Hao Hu[1], Christopher McFarlane[3]

[1]State Key Laboratory of Geological Processes and Mineral Resources, and Faculty of Earth Resources, China University of Geosciences, Wuhan 430074, China
[2]Department of Earth Sciences, the University of Hong Kong, Hong Kong SAR, China
[3]Department of Earth Sciences, University of New Brunswick, Fredericton, NB E3B 5A3, Canada

*Corresponding author
Email: xfzhao@cug.edu.cn

Always consult and cite the final, published document. See http:/www.minsocam.org or GeoscienceWorld

ABSTRACT

Metasomatic alteration of fluorapatite has been reported in several iron-oxide apatite (IOA) deposits, but its effect on elemental and isotopic variations has not been well understood. In this study, we present integrated elemental, U-Pb, Sr, and O isotopic microanalytical data on fresh and altered domains in fluorapatite from the Taocun IOA deposit, Eastern China, to evaluate the timing and nature of the metasomatism and its effects on the ore-forming event. Orebodies of the Taocun deposit are spatially associated with a subvolcanic, intermediate intrusion, which displays zonal alteration patterns with albite in the center and increasing actinolite, chlorite, epidote, and carbonate towards the margin. Both disseminated and vein-type ores are present in the Taocun deposit, and fluorapatite commonly occurs with magnetite and actinolite in most ores.

Fluorapatite grains from the both types of ores have been variably metasomatized through a coupled dissolution-reprecipitation mechanism. Many trace elements, including Na, Cl, S, Si, Mg, Sr, U, Th, and (REEs+Y), were variably leached from the fluorapatite grains during this process and the Sr and O isotopic signatures of the grains were also modified. The altered fluorapatite grains/domains have *in-situ* $^{87}Sr/^{86}Sr$ ratios (0.70829 to 0.70971) slightly higher than those of the fresh fluorapatite (0.70777 to 0.70868), and $\delta^{18}O$ values (-3.0 to +3.4 ‰) variably lower than the primary domains (+5.3 to +7.5 ‰). The Sr and O isotopes of the primary fluorapatite are consistent with or slightly higher than those of the ore-hosting intrusion, implying that the early-stage, ore-forming fluids were magmatic in origin but underwent weak interaction with the country rocks.

U-Pb dating of the fresh and altered domains of the fluorapatite yielded indistinguishable ages of ~131 Ma, which are the same as the age of the ore-hosting intrusion. In combination with fluid inclusion data, we propose that the metasomatism of fluorapatite was induced by hydrothermal fluids at a late stage of the ore-forming event. The shifts to higher $^{87}Sr/^{86}Sr$ ratios and lower $\delta^{18}O$ values in the altered fluorapatite indicate that the alteration was induced by fluids with more radioactive Sr

Always consult and cite the final, published document. See http:/www.minsocam.org or GeoscienceWorld

and lighter O isotope signatures. The metasomatic fluids were likely dominated by meteoric waters that were mixed with the earlier magmatic fluids and interacted with sedimentary rocks. Our study highlights that elemental and isotopic compositions of fluorapatite can be significantly modified by hydrothermal fluids during ore-forming events. Thus, instead of traditional bulk-rock analysis, *in-situ* microanalysis is important to provide accurate constraints on the magmatic and/or hydrothermal evolution of complex ore-forming systems.

Key words: fluorapatite, microanalysis, fluid metasomatism, SIMS oxygen isotope, IOA deposit

Always consult and cite the final, published document. See http:/www.minsocam.org or GeoscienceWorld

This is a preprint, the final version is subject to change, of the American Mineralogist (MSA)
Cite as Authors (Year) Title. American Mineralogist, in press.
(DOI will not work until issue is live.) DOI: http://dx.doi.org/10.2138/am-2016-5743

INTRODUCTION

Apatite is a common mineral in a variety of hydrothermal deposits, including iron-oxide copper gold, skarn, and porphyry Cu-Au deposits (e.g., Belousova et al. 2002; Pan and Fleet 2002; Zhao et al. 2015), and is a major constituent of iron-oxide apatite (IOA) deposits (e.g., Frietsch and Perdahl 1995). It normally contains a variety of trace elements (e.g., halogens, S, Fe, Mn, Sr, and rare earth elements (REEs)), which can be used to document the mineralizing conditions. In addition, Sr and O isotopes of apatite can be effectively employed to trace the source and evolution of the ore-forming fluids (e.g., Li and Zhou 2015; Zhao et al. 2015). Furthermore, apatite is a good host for fluid inclusions, which can directly reflect the nature of ore-forming fluids (e.g., Jami et al. 2007; Nabatian and Ghaderi 2013; Li et al. 2015). Thus, apatite is an ideal phase for the study of ore genesis and the evolution of hydrothermal deposits.

However, it has been documented that apatite can be partially or completely metasomatically altered by hydrothermal fluids (e.g., Harlov et al. 2002; Harlov and Förster 2003; Harlov et al. 2005; Chen and Zhou 2015; Li and Zhou 2015; Harlov 2015), which raises questions about the interpretation of elemental and isotopic compositions. Fluid metasomatism usually leads to significant remobilization of trace elements, and the formation of new REE phosphates (e.g., monazite and xenotime) in the altered zones. Experimental studies have demonstrated that fluid metasomatism commonly occurs via a coupled dissolution-reprecipitation mechanism, and that the formation of new REE mineral phases is induced by Na- and Ca-deficit fluids (Harlov et al. 2002; Harlov and Förster 2003; Harlov et al. 2005). However, the sources and characteristics of metasomatic fluids in hydrothermal ore deposits, are much more complex than laboratory experiments, and thus are not well understood (e.g., Bonyadi et al. 2011; Li and Zhou 2015). So it is important to understand better the mechanism and processes of the metasomatism. The development of micro-analytical techniques has now made it possible to examine intracrystalline and sub-grain scale compositional variations and thus, allows us to decipher elemental and isotopic changes between reactant and product phases. This can greatly enhance our

Always consult and cite the final, published document. See http:/www.minsocam.org or GeoscienceWorld

understanding of metasomatic processes, as well as their geological implications.

Metasomatic alteration of fluorapatite is known to be widespread in IOA deposits (e.g., Harlov et al. 2002; Torab and Lehmann 2007; Bonyadi et al. 2011). However, such metasomatism could have been related to either the ore-forming events (e.g., Harlov et al. 2002; Torab and Lehmann 2007; Chen and Zhou 2015; Li and Zhou 2015) or could have occurred many millions of years later during post-ore hydrothermal or metamorphic events (e.g. Stosch et al. 2011; Li and Zhou 2015). Dating of the metasomatic event is hence crucial to understanding the sources of the metasomatic fluids and their geological implications. This paper presents systematic petrographic, elemental, and isotopic data for fluorapatite from the Taocun deposit, a representative IOA deposit from the Middle-Lower Yangtze River Valley Metallogenic Belt (MLYRVMB), East China. Major and trace element compositions, as well as *in-situ* U-Pb, Sr, and O isotopic ratios, were determined on fresh and altered domains of the fluorapatite grains. This comprehensive dataset indicates that the fluorapatite grains were variably metasomatized by hydrothermal fluids during a late stage of the ore-forming event, and hence provide a detailed record of fluid evolution in the system. The results of this study also highlight the potential of *in-situ* analytical techniques for providing more effective and accurate constraints on the evolution of ore-forming systems.

GEOLOGICAL BACKGROUND

The MLYRVMB is located in the northeastern part of the Yangtze Block, just south of the Qinling-Dabie orogenic belt (Fig. 1). It hosts seven mining districts, which contain skarn and porphyry Cu-Au deposits (145-135 Ma), and slightly younger IOA deposits (ca.130 Ma) (e.g., Ishihara et al. 1986; Xu 1990; Zhai et al. 1992; Tang et al. 1998; Pan and Dong 1999; Hou and Yuan 2010; Yuan et al. 2010; Mao et al. 2011; Zhou et al. 2011, 2013). The most important IOA deposits are located in the Ningwu ore district in the eastern MLYRVMB (Fig. 1b). The Ningwu ore district lies in an early Cretaceous volcanic basin, whose development was controlled by NE-striking regional faults (Fig. 2). The stratigraphic sequence and volcanic rocks

Always consult and cite the final, published document. See http:/www.minsocam.org or GeoscienceWorld

of the Ningwu basin have been described in detail by previous investigators (e.g., Ningwu Research Group 1978; Xu 1990; Pan and Dong 1999). The sequence consists of a thick section of early Cretaceous volcanic rocks that unconformably overlie lower-middle Triassic platform carbonates and middle-upper Jurassic, continental, clastic sedimentary rocks (Ningwu Research Group 1978). From the base upward, the early Cretaceous volcanic rocks are divided into the Longwangshan, Dawangshan, Gushan, and Niangniangshan formations (Fig. 2). The basal Longwangshan Formation, which is mainly composed of andesitic to trachyandesitic volcanic breccia, tuff, lava, and intercalated siltstone, has zircon U-Pb ages of 131 Ma to 133 Ma (Zhang et al. 2003; Zhou et al. 2011). The Dawangshan Formation consists predominantly of trachyandesitic lava, locally accompanied by breccia and tuff in the northern and central parts of the basin. It constitutes the major component of the volcanic basin and has zircon U-Pb ages of 130 Ma to 132 Ma (Zhang et al. 2003; Hou and Yuan 2010; Zhou et al. 2011). The Gushan Formation is exposed only in the southern part of the basin (Fig. 2), where it consists of a basal sequence of clastic sedimentary rocks overlain by trachyandesitic lava, breccia, and tuff with zircon U-Pb ages of 128 Ma to 130 Ma (Hou and Yuan 2010; Zhou et al. 2011). The uppermost Niangniangshan Formation consists of phonolite and phonolitic tuff with a zircon U-Pb age of ca. 127 Ma (Zhou et al. 2011).

The volcanic rocks of the lower two formations host numerous subvolcanic intrusions (Figs. 2 and 3), which have zircon U-Pb ages of 130 Ma to 131 Ma (e.g., Duan et al. 2011; Hou et al. 2012; Zhou et al. 2013) and are considered to be roughly contemporaneous with the Dawangshan volcanic cycle. These subvolcanic intrusions commonly have porphyritic textures and most are thought to have been emplaced at depths of <1km from the paleosurface (Ningwu Research Group 1978). They are geochemically similar to the volcanic rocks of the Dawangshan cycle, and traditionally have been described as pyroxene-bearing diorite porphyries (Ningwu Research Group 1978). These intrusive rocks are characterized by high alkali contents (Na_2O+K_2O=4.8-9.1 wt.%; Ningwu Research Group 1978), placing them in the shoshonite series. Granitic intrusions, including quartz monzonite and granite, are also

Always consult and cite the final, published document. See http:/www.minsocam.org or GeoscienceWorld

158 locally present within the volcanic basin (Fig. 2) and have zircon U-Pb ages of 130
159 Ma to 126 Ma (Yuan et al. 2011). No significant regional metamorphism or
160 deformation occurred after formation of the volcanic basin.

161 More than 30 IOA deposits are known in the Ningwu ore district, with a total
162 confirmed resource up to 2700 Mt Fe-oxides (Masteel Mining Co. Ltd. 2012). All the
163 deposits are spatially and temporally associated with the subvolcanic dioritic
164 intrusions (Fig. 2). Orebodies are mainly hosted within the apical zones of the
165 intrusions and/or along the contacts between the intrusions and country rocks. Several
166 geochronological studies have demonstrated that ore mineralization was coeval with
167 the emplacement of the subvolcanic intrusions at ca. 130 Ma (e.g., Fan et al. 2010;
168 Yuan et al. 2010; Duan et al. 2011; Zhou et al. 2011).
169
170 ## GEOLOGY OF THE TAOCUN IOA DEPOSIT

171 The Taocun deposit, located in the central part of the Ningwu basin, is one of
172 numerous typical IOA deposits in the region (Fig. 2). Ore mineralization was
173 genetically related to emplacement of a subvolcanic dioritic intrusion, which was
174 overlain by volcanic rocks of the Dawangshan Formation (Figs. 3 and 4; Ningwu
175 Research Group 1978). The orebodies are mainly hosted within the apical zone of the
176 extensively altered intrusion. The ore zone, which is approximately 1000-1600 m long,
177 500 m wide, and 10-150 m thick, contains 360 Mt ore at an average grade of 20-26
178 wt.% Fe, 0.06-0.17 wt.% V, 0.32-3.96 wt.% S, and 0.01-3.08 wt.% P (Masteel Mining
179 Co. Ltd. 2012). Most of the individual ore bodies strike NE and are stratiform or
180 lens-shaped in cross section (Fig. 4).

181 ### Mineralization and hydrothermal alteration

182 The Taocun deposit consists mainly of two types of ore: (1) disseminated ore that
183 is composed of magnetite, apatite, actinolite, albite and epidote (Fig. 5a-5b and 5e),
184 and (2) vein-type ore that contains coarse-grained to pegmatitic,
185 magnetite-actinolite-apatite assemblages (Fig. 5c-5f). Disseminated ores constitute the
186 major orebody, whereas vein-type ores are locally developed along fractures or joints
187 in the ore-hosting intrusion. Magnetite-actinolite-apatite veins commonly fill fractures

Always consult and cite the final, published document. See http:/www.minsocam.org or GeoscienceWorld

188 in both the disseminated ores and altered intrusive rocks (Fig. 5d and 5e), suggesting
189 that the vein-type mineralization postdated the disseminated mineralization. Both
190 types of ores have magnetite, apatite, and actinolite as the major phases (Figs. 5 and
191 6).

192 Hydrothermal alteration is extensive in the Taocun deposit and has a well-defined
193 spatial zonation (Fig. 4). The inner zone of pervasive sodic alteration occurs mainly
194 within the ore-hosting intrusion. The sodic alteration (stage I) consists mainly of albite
195 and scapolite (Fig. 7), which was overprinted by interstitial magnetite (Fig. 5a).
196 Precipitation of disseminated magnetite likely commenced during the waning stage of
197 sodic alteration marked by marialitic scapolite (Fig. 5a). Magnetite is mostly
198 intergrown with apatite and diopside/actinolite (Fig. 6a and 6b), suggesting these are
199 coeval products of stage II alteration. Stage III sodic-calcic alteration, which postdates
200 deposition of the disseminated magnetite, consists of albite, actinolite, epidote, and
201 chlorite, and is particularly abundant at the intermediate alteration zone (Fig. 4). It
202 was probably responsible for the observed pseudomorphic replacement of scapolite by
203 albite (Fig. 5a) and diopside by actinolite. Quartz and carbonate minerals (siderite and
204 calcite) mark the last stage (IV) of alteration (Fig. 5e), which is most extensive in the
205 outer zone within the volcanic rocks (Fig. 4). Kaolinite occurs locally along the
206 contact between the volcanic rocks and the intrusion (Fig. 4).

207 Vein-type mineralization also produced four stages (i to iv; Fig. 7) of alteration.
208 However, the alteration is localized or confined to zones along the margins of
209 magnetite-apatite veins. Vein-type magnetite ores typically have alteration halos at the
210 contacts with the country rocks (Fig. 5d and 5e). Stage i sodic alteration was relatively
211 weak in the magnetite ore veins. Magnetite was deposited synchronously with
212 well-crystallized apatite and diopside/actinolite in stage ii (Figs. 5c-5d, 5f and 6c-6d),
213 which was then overprinted by epidote and chlorite of stage iii. Stage iii alteration
214 differs from that in the disseminated ores by the presence of anhydrite (Fig. 7) and the
215 absence of albite. Anhydrite and/or pyrite veins of stage iv commonly crosscut both
216 disseminated and vein-type magnetite ores (Fig. 5f).

217

Always consult and cite the final, published document. See http:/www.minsocam.org or GeoscienceWorld

SAMPLES AND METHODS

Apatite samples from both the disseminated and vein-type ores were collected for textural, elemental, and isotopic analyses. Both normal (30-40 μm) and thick (100-120 μm) double-polished thin sections were made. Normal thin sections were used for petrographic observation, whereas thick sections were used for laser ablation analysis. The textures of all samples were examined in detail using scanning electron microscopy (SEM) and/or optical cathodoluminescence (OP-CL), prior to the *in-situ* elemental and isotopic analyses.

Optical cathodoluminescence (CL) microscopy

Optical CL photomicrography was carried out on polished sections using an Olympus Vanox microscope coupled with a Relion III CL system, at the Faculty of Earth Resources, China University of Geosciences (Wuhan). The low vacuum Relion system was set to an electron source operated at 15–20kV and about 500–800μA.

Electron microprobe (EMP) analysis

Quantitative EMP analyses were performed using a JXA-8230 Superprobe equipped with wavelength-dispersive spectrometers at the Center of Material Research and Analysis, Wuhan University of Technology (WUT). The instrument was set to operate at an accelerating voltage of 15 kV and a beam current of 20 nA. The standards used in this study included: albite for Na, almandine for Si, fluorapatite for Ca and P, hematite for Fe, chrome-diopside for Mg, rhodonite for Mn, celestine for Sr, barite for S, bababudanite for Cl, and fluorite for F. Data were corrected using the internal ZAF correction program (Armstrong 1991). Oxygen was calculated from cation stoichiometry, and the apatite chemical formula calculation was based on 8 cations.

LA-ICPMS trace element analysis

Trace elements of apatite were analyzed *in-situ* using laser ablation inductively coupled-plasma mass spectrometry (LA-ICP-MS) at the Guangzhou Institute of Geochemistry, Chinese Academy of Sciences. The Agilent7500a ICP-MS instrument was coupled to a Resonetics RESOlution M-50 laser-ablation system. Analytical procedures and instrumental operating conditions are fully described by Tu et al. (2011). Each spot analysis involved 40s data acquisition and 20s background measurement using a laser repetition rate of 4 Hz and a beam of ~33μm. CaO content determined by EMPA was employed as an internal standard for data calibration using ICPMSDataCal (Liu et al. 2008). Reference material NIST 610 was used as an external standard

Always consult and cite the final, published document. See http:/www.minsocam.org or GeoscienceWorld

to correct drift. The analytical uncertainty is better than 10% (relative percentage) for most trace elements.

LA-MC-ICPMS Sr isotopic analysis

In-situ Sr isotopic analyses of apatite were performed on 100-120-μm-thick double-polished sections, using a Neptune Plus MC-ICP-MS connected with a Newwave UP193 laser ablation system at the State Key Laboratory of Mineral Deposit Research, Nanjing University. Instrumental operating conditions and data acquisition protocols are described in Ramos et al. (2004), Yang et al. (2009b), and Gao and Zhou (2013), and are briefly summarized here. For each sample, data acquisition consisted of ~40 s ablation using spot sizes of 150 μm with a repetition pulse rate of 5 to 10 Hz depending upon Sr contents. Previous studies have shown that spot sizes and repetition rates do not affect the accuracy of the Sr isotope data, but do influence the precision of the data (SD) (Yang et al. 2009a; Wu et al. 2010). The natural Kr ratios of $^{83}Kr/^{84}Kr$ = 0.20175 and $^{83}Kr/^{86}Kr$ = 0.66474 are assumed for overlap correction. The natural ratio of $^{85}Rb/^{87}Rb$ (2.5926) was used for correction of isobaric Rb interference by the exponential law, assuming that Rb has the same mass discrimination as Sr. Interference from the bivalent rare earth elements (REEs) was also considered due to the potentially high concentrations of REEs in apatite. As proposed by Ramos et al. (2004), the presence of $^{167}Er^{2+}$, $^{171}Yb^{2+}$ and $^{173}Yb^{2+}$ at masses 83.5, 85.5, and 86.5 was monitored. Then the contributions of $^{168}Er^{2+}$ and $^{168}Yb^{2+}$ to ^{84}Sr, $^{170}Er^{2+}$ and $^{170}Yb^{2+}$ to ^{85}Sr ($+^{85}Rb$), $^{172}Yb^{2+}$ to ^{86}Sr, $^{174}Yb^{2+}$ to ^{87}Sr ($+^{87}Rb$), and $^{176}Yb^{2+}$ to ^{88}Sr were calculated according to the isotopic abundances of Er and Yb. The in-house apatite standard (LAP, from Afghanistan) was used to evaluate the reliability of the analytical accuracy and the potential matrix-matched effect during analyses (Gao and Zhou 2013). During our analyses, the standard yielded an average $^{87}Sr/^{86}Sr$ ratio of 0.71137 ± 0.00003 (2SD) (n=23), which was highly consistent with values of 0.71137 ± 0.00007 and 0.71138 ± 0.00004 obtained by *in-situ* LAMC-ICP-MS and chemically purified solutions (MC-ICP-MS) methods, respectively (Yang et al. 2009b). The Sr content was not acquired due to the lack of an internal standard. However, ^{88}Sr (Volt) (^{88}Sr ion signal intensity) can be used for comparison of Sr abundances of different samples.

SIMS O isotopic analysis

For SIMS oxygen isotope analysis, separated apatite grains from disseminated ores and small pieces drilled from the polished thick sections of vein-type apatite, were embedded in epoxy discs

Always consult and cite the final, published document. See http:/www.minsocam.org or GeoscienceWorld

278 together with apatite standards (Qinghu and Durango). *In-situ* O isotopes were obtained using a
279 Cameca IMS-1280 at the Institute of Geology and Geophysics, Chinese Academy of Sciences. The
280 analytical procedures were similar to those used for zircon oxygen isotopes as described by Li et
281 al. (2010). The Cs^+ primary ion beam was accelerated at 10 kV, with an intensity of ~2 nA, with
282 spot sizes of about 20 μm in diameter. The normal-incidence electron flood gun was used to
283 compensate for the charge at the surface of the gold-coated samples. The ^{16}O and ^{18}O ion
284 intensities were measured simultaneously in multi-collection mode using two off-axis Faraday
285 cups. The relative 2σ-errors given for the $\delta^{18}O$ analyses include both external and internal
286 precision. The values of $\delta^{18}O$ were standardized to Vienna Standard Mean Ocean Water
287 compositions (V_{VSMOW}), reported in standard per mil notation, and corrected for the instrumental
288 mass fractionation factor (IMF). The IMF was obtained using the Durango fluorapatite as a
289 reference with $\delta^{18}O$ value of 9.4 ‰ (Trotter et al. 2008). The Qinghu apatite was also analyzed as
290 external reference in this study and yielded an average value of 4.4 ± 0.2 ‰. The external
291 reproducibility of $^{16}O/^{18}O$ ratios by repeated measurements of the standard was better than
292 0.27 ‰.

293 **Bulk analysis of apatite O isotopes**

294 To compare with *in situ* SIMS oxygen isotopic results, pure apatite separates were handpicked
295 from disseminated ore samples (NW-88 and NW-99) and vein-type ore sample (NW-18) after
296 crushing. Sample NW-18 contains apatite of two colors; one domain is clear and transparent; the
297 other domain is reddish possibly due to hematite inclusions. Apatite grains of both colors were
298 handpicked separately. Mineral separates of all samples were more than 99% pure apatite.

299 The oxygen isotopic compositions of apatite separates were determined at the US Geological
300 Survey laboratories in Denver using the conventional fluorination procedure of Clayton and
301 Mayeda (1963). Aliquots of 10 ± 5 mg apatite were reacted with Br pentafluoride in sealed nickel
302 vessels at 575°C and converted to CO_2 by reaction with an internally heated carbon rod (Clayton
303 and Mayeda 1963). Isotopic analyses were performed using a Finnigan MAT 252, and all data
304 were reported in per mil relative to V_{VSMOW} and expressed as delta (δ) values. Repeated analyses
305 of the NBS-28 standard gave a value of 9.7 ± 0.2 ‰ (2σ).

306 **LA-ICPMS U-Pb isotope analysis**

307 *In-situ* U-Pb analysis of fluorapatite was carried out using a Resonetics M-50 193 nm ArF

Always consult and cite the final, published document. See http:/www.minsocam.org or GeoscienceWorld

(excimer) laser ablation system coupled with an Agilent 7700x quadrupole ICP-MS at the Department of Earth Sciences, University of New Brunswick. A combination of 2.0 mL/min N_2 added to the He + Ar carrier gas and the use of a second external rotary pump improved high mass sensitivity. Laser fluence was regulated at ~6 J/cm^2. The ICP-MS was first tuned using NIST610 to acquire oxide production (monitored as $^{248}ThO^+/^{232}Th^+ < 0.3\%$) and U/Th ($^{238}U^+/^{232}Th^+ \approx 1.05$) values, whereas bivalent ion production (measured as $^{22}M^+/^{44}Ca^+$) was not strictly monitored. Samples were ablated using 47 µm diameter spots and a repetition frequency of 3 Hz to minimize laser-induced Pb/U fractionation. Acquisition time for each spot analysis consisted of ~30 s background and ~30 s ablation. The MAD apatite standard was utilized for external standardization to correct for laser-induced Pb/U fractionation and mass discrimination in the ICP-MS (Thomson et al. 2012). Element concentrations were calibrated against NIST610, which was analysed periodically throughout the ablation sequence. The analyzing dwell times (in milliseconds) chosen were: ^{43}Ca (10), ^{31}P (10), ^{202}Hg (50), ^{204}Pb (70), ^{206}Pb 50), ^{207}Pb (70), ^{208}Pb (15), ^{232}Th (10), and ^{238}U (15). Data quality was monitored by repeated measurement of in-house standard FC-1 apatite. Off-line selection and integration of background and analysis signals, and time-drift correction and quantitative calibration for U-Pb dating were performed by Iolite and VizualAge (Paton et al. 2011; Petrus and Kamber 2012). The Tera-Wasserburg diagram and weighted mean calculations were obtained using Isoplot/Ex_ver3 (Ludwig 2003). Apatite commonly contains a significant amount of common Pb (e.g. Chew et al. 2011). Plots of Tera-Wasserburg diagrams using the isotopic ratios without common Pb correction, and ^{207}Pb corrected $^{206}Pb/^{238}U$ ages were calculated using an initial $^{207}Pb/^{206}Pb$ ratio of 0.852 ± 0.068 from the ore-hosted intrusion (Xing 1996).

PETROGRAPHY

For simplicity, fluorapatite from the disseminated and vein-type ores is hereafter named as disseminated and vein fluorapatite, respectively.

Disseminated fluorapatite

Disseminated fluorapatite grains are widely distributed, but are difficult to identify in hand specimen due to their small grain size and similarity in color to albite (Fig. 5b and 5e). They commonly occur as subhedral to anhedral grains, and are closely

Always consult and cite the final, published document. See http:/www.minsocam.org or GeoscienceWorld

associated with magnetite and actinolite, all of which may be overprinted by albite, chlorite, and epidote (Figs. 6a-6b and 7).

Under BSE imaging, the fluorapatite grains commonly show textures of fluid metasomatism. The unaltered/primary domains are relatively homogeneous and bright, whereas the altered domains are variably darker than the precursors (Figs. 6a-6b and 8a-8f). The altered grains are characterized by pitted surfaces with visible voids and mineral inclusions, including monazite, allanite, and albite (Fig. 8a-8f). In some grains, monazite inclusions are elongate and show a preferred orientation along crystallographic lattice planes of the apatite (Fig. 8f). The unaltered domains have primary needle-shaped fluid inclusions, which are parallel to the c-axis of the host grain (Fig. 8g). In contrast, fluid inclusions in the altered zones are oblate in shape and randomly distributed (Fig. 8g). The altered zones contain abundant aqueous fluid inclusions (Fig. 8g-8i) and/or negative crystal-shaped daughter minerals, commonly halite and an unknown mineral (Fig. 8h and 8i).

Vein fluorapatite

In hand specimen, vein fluorapatite crystals are usually yellowish-green in color with some pegmatitic crystals ranging from yellowish-green to red (Fig. 5c). They commonly form euhedral to subhedral grains closely associated with magnetite and actinolite (Fig. 6c and 6d). Similar to the disseminated fluorapatite, vein-type grains have also been altered by metasomatic fluids. In BSE images, the altered domains are darker than the unaltered domains (Figs. 6c-6d and 9c-9i). In microscopic CL images, the blue-colored domains correspond to BSE-bright domains (viz. unaltered zones), whereas light green domains correspond to BSE-dark domains (viz. altered zones) (Fig. 9b and 9c). The altered domains in vein fluorapatite tend to occur along rims and brittle fractures, or as irregular stripes and patches in the interior of the pristine phases (Fig. 9). The altered domains contain many voids and may host minor monazite and anhydrite inclusions (Fig. 9). Allanite has also been identified in the altered domains, where it mostly occurs along intracrystalline brittle fractures (Fig. 9e, 9g and 9i). Anhedral quartz and calcite also occur in the altered domains (Fig. 9d, 9f and 9h) where they most likely formed by metasomatic processes. However, these minerals

Always consult and cite the final, published document. See http:/www.minsocam.org or GeoscienceWorld

may also have formed by post-replacement processes, because quartz-calcite veins locally crosscut both unaltered and altered fluorapatite crystals (Fig. 9e-9f and 9i).

RESULTS

Chemical composition of fluorapatite

Fluorapatite from the Taocun deposit contains 2.16–3.16 wt.% F and <1.0 wt.% Cl (Appendix Table 1), but the fresh and altered grains have distinct compositions. In general, the altered grains/domains have contents of Cl, Si, S, Mg, Fe, Sr, V, U, Th, and REEs lower than the unaltered domains in both disseminated and vein fluorapatite (Figs. 10-11; Appendix Tables 1 and 2).

In addition to P_2O_5 (41.57–43.41 wt.%), CaO (53.41–54.37 wt.%), and F (2.24–2.90 wt.%), the unaltered domains of disseminated fluorapatite also contain minor Cl (0.35–0.97 wt.%), Na_2O (0.10–0.17 wt.%), and SO_3 (0.25–0.52 wt.%). Compared to the unaltered domains, the altered domains contain lower Cl (< 0.50 wt.%), Na_2O (< 0.06 wt.%), and SO_3 (< 0.27 wt.%) (Fig. 10a; Appendix Table 1). The altered domains also have lower Si, Mg, Sr, V, and Fe than the unaltered domains (Fig. 10b and 10e-10f). In terms of trace element data, the REEs (total REE = 6375 to 10092 ppm) and Y (441 to 572 ppm) contents in unaltered domains are much higher than those of altered domains (total REE = 1619–2795 ppm, Y = 170–235 ppm) (Appendix Table 2). It is notable that Si and (REE+Y) in both altered and unaltered domains show a linear positive correlation (Fig. 10b), indicating that ($REE^{3+} + Y^{3+}$) are incorporated into the disseminated fluorapatite crystal structure following the coupled substitution reaction (Pan and Fleet 2002):

$$Si^{4+} + (REE+Y)^{3+} = P^{5+} + Ca^{2+}$$

Even though the unaltered and altered domains have different REE contents (Fig. 10b and 10c), they display similar LREE-enriched chondrite-normalized patterns, with moderately negative Eu anomalies (Fig. 11; Appendix Table 2). There is also a significant decrease of Th and U contents from the unaltered to the altered domains (Fig. 10d), particularly for Th (decreasing from 122–328 ppm to 9.39–70.4 ppm).

Apart from P_2O_5 (41.98–43.83 wt.%), CaO (53.46–55.13 wt.%), and F (2.29–2.98

Always consult and cite the final, published document. See http:/www.minsocam.org or GeoscienceWorld

wt.%), both the unaltered and altered vein fluorapatite contains minor SO_3 (< 0.67 wt.%), Na_2O (< 0.24 wt.%), and FeO (< 0.12 wt.%) (Appendix Table 1). It is notable that the unaltered domains are relatively enriched in SO_3 (0.35–0.57 wt.%) and Na_2O (0.11–0.24 wt.%), and exhibit a positive correlation between S and Na atoms (Fig. 10a), suggesting the following coupled substitution reaction (Pan and Fleet 2002):

$$Na^{+} + S^{6+} = Ca^{2+} + P^{5+}$$

Regarding trace elements obtained by LA-ICPMS, fresh vein fluorapatite domains commonly contain trace elements higher than those in altered domains (Fig. 10). For example, the altered domains have lower contents of Th (8.3–45.3 ppm) and U (≤ 2.1 ppm) than the unaltered domains with Th (97.7–191 ppm) and U (6.9–12.7 ppm) (Fig. 10d). The altered domains also have LREE contents and La_N/Yb_N ratios ($La_N/Yb_N \leq$ 22.6) lower than the unaltered domains, but their HREE concentrations are in almost the same range (Figs. 10c and 11b; Appendix Table 2). There is one exception, NW18 Apt-5, in which the total REE elements are depleted (Fig. 11b).

Sr isotopes of fluorapatite

Due to high Sr (> 252 ppm) and extremely low Rb (< 1.38 ppm) concentrations in the fluorapatite (Appendix Table 2), the present-day $^{87}Sr/^{86}Sr$ ratios of the grains could be considered as the initial Sr isotopic signatures. The unaltered disseminated fluorapatite has $^{87}Sr/^{86}Sr$ ratios (0.70802–0.70868) almost identical to those of the vein fluorapatite (0.70777–0.70828) (Fig. 12; Table 1). The altered disseminated grains have obviously higher $^{87}Sr/^{86}Sr$ ratios (0.70880–0.70971) than the unaltered grains. Analyses on altered domains of vein fluorapatite $^{87}Sr/^{86}Sr$ ratios (0.70829–0.70848) are slightly higher than those in the unaltered domains, but three exceptions have obviously higher ratios (0.70908–0.70956) (Fig. 12; Table 1).

Oxygen isotopes of fluorapatite

In-situ SIMS O isotopes were performed on both unaltered and altered domains of fluorapatite. To evaluate the effect of metasomatism on oxygen isotopes, conventional bulk analyses of fluorapatite were conducted to compare with the SIMS data. Unaltered domains of disseminated fluorapatite have $\delta^{18}O$ values (+5.7 to +7.0 ‰) much higher than the altered zones (-3.0 to +3.1 ‰) (Fig. 13; Table 2). In contrast, the

Always consult and cite the final, published document. See http:/www.minsocam.org or GeoscienceWorld

bulk analyses of fluorapatite separates have $\delta^{18}O$ values of +2.06 ‰ (NW-88) and +1.65 ‰ (NW-99) (Table 3), which plot within the range of the SIMS data of the altered domains (Fig. 13). Vein fluorapatite grains have oxygen isotopes similar to those of disseminated fluorapatite. Unaltered domains have $\delta^{18}O$ values ranging from +5.3 to +7.5 ‰, whereas the altered zones have much lower values of -0.3 to +3.4 ‰ (Fig. 13; Table 2). Bulk analysis of two vein fluorapatite separates (NW-18) yields $\delta^{18}O$ values of +4.10 ‰ (reddish grains) and 5.2 ‰ (transparent grains) (Table 3).

U-Pb dating of fluorapatite

Both unaltered and altered domains of vein fluorapatite were analyzed using the LA-ICPMS U-Pb method. The U-Pb data are summarized in Table 4, and are graphically shown in Fig. 14. The unaltered domains have 116–224 ppm Th, 23.5–84.0 ppm U, and Th/U ratios of 14.8–22.4, whereas the altered domains have obviously lower Th (≤ 10.5 ppm) and U (≤ 4.3 ppm). The Tera-Wasserburg plots use the common Pb uncorrected data but the intercept was anchored through an initial $^{207}Pb/^{206}Pb$ ratio of 0.852 ± 0.068 for the ore-hosting intrusion (Xing 1996). Forty-one spot analyses have an intercept age of 131.2 ± 2.2 Ma (MSWD = 2.2), which is indistinguishable from the intercept U-Pb age (131.2 ± 1.9 Ma, MSWD = 1.6) using thirty-two analyses from the unaltered domains only (Fig. 14a). The two ages are also consistent with the ^{207}Pb corrected weighted mean $^{206}Pb/^{238}U$ age of 131.1 ± 1.9 Ma (MSWD = 1.6; Fig. 14b) for unaltered grains. Due to the low concentrations of U and Pb, and much higher percentage of common Pb, most analyses from the altered domains did not yield meaningful ^{207}Pb corrected $^{206}Pb/^{238}U$ ages (Table 4).

DISCUSSION

Fluid-aided, coupled dissolution-reprecipitation processes in metasomatic alteration of fluorapatite

The data presented above show that fluorapatite from both types of ores underwent extensive metasomatic alteration. The altered fluorapatites in the both types of ores have the following features (Figs. 6 and 8-13): (1) the altered domains preserve the shape and orientation of the primary crystals; (2) there are sharp compositional

Always consult and cite the final, published document. See http:/www.minsocam.org or GeoscienceWorld

458 boundaries at interfaces between the unaltered crystal and the altered domains; (3)
459 pervasive micro-porosities and fluid inclusions are present in altered domains; and (4)
460 the oxygen isotopes in framework structures of the unaltered and altered domains are
461 systematically different, implying that new structural P-O bonds formed during
462 formation of the altered domains. All these observations are consistent with a
463 fluid-aided, coupled dissolution-reprecipitation process. Fluid-aided, coupled
464 dissolution-reprecipitation is a well-established chemical reaction, during which a
465 mineral phase, in the presence of a reactive fluid, is replaced either by the same phase
466 with a new composition or by an entirely new phase (cf., Putnis 2002, 2009). During
467 dissolution-reprecipitation, the original and new phases are separated by a thin, fluid
468 film with a thickness generally on a submicron scale (cf., Putnis 2002, 2009).
469 Elements can be transported from the dissolving phases across the fluid-filled reaction
470 front to the reprecipitating phases. As a result, the basic atomic framework of the
471 original phase is destroyed, and a sharp reaction interface forms between the two
472 phases. Moreover, interconnected micro- (and nano-) porosity and fluid inclusions
473 develop in the reprecipitated phases due to a combination of molar volume change
474 and slight differences in solubility between parent and product phases (cf., Putnis
475 2002, 2009). In turn, increased porosity, and the presence of fluid inclusions inside the
476 altered crystals, will enhance chemical exchanges between the interior of the crystal
477 and the reactive fluid system, which allows for re-equilibration between mineral and
478 fluid.

479 As a consequence of metasomatism, there are complex chemical exchanges
480 between fluorapatite and the reactive fluids. The most obvious feature is the leaching
481 of many trace elements, including REEs, Na, Si, S, Fe, Mg, Sr, V, U, and Th (Figs. 10
482 and 11), which is in good agreement with experimental studies and other
483 metasomatized natural samples (e.g., Harlov et al. 2002; Harlov and Förster 2003;
484 Harlov et al. 2005; Li and Zhou 2015). Parts of the leached REEs should have been
485 immediately reprecipitated into the new phases, thereby producing monazite and
486 allanite inclusions in close association with the altered domains (Figs. 8 and 9). It is
487 notable that the altered domains have Sr isotopic compositions higher than the

Always consult and cite the final, published document. See http:/www.minsocam.org or GeoscienceWorld

unaltered fluorapatite (Fig. 12). This implies that, although the Sr content was largely leached out of the metasomatized fluorapatite (Fig. 10e), changes in isotopic ratios occurred between the metasomatized fluorapatite and the reactive fluids. The isotopic exchange between fluorapatite and the metasomatic fluid was further confirmed by *in situ* oxygen isotopic data, i.e., the altered domains have a range of $\delta^{18}O$ values variably lower than the fresh domains (Fig. 13). The significant elemental and isotopic changes during the metasomatism imply that the chemical compositions of the unaltered and altered domains of fluorapatite can be used to document the conditions of primary ore-forming fluids and later metasomatic fluids, respectively.

Characteristics of the metasomatic fluids

Although the disseminated and vein fluorapatite show many similarities, they also show different characteristics in terms of mineral inclusions, as well as elemental and isotopic changes in the altered domains. Field relationships show that the vein-type ores formed slightly later than the disseminated ores (Fig. 5d and 5e). Thus, the metasomatic processes and nature of the reactive fluids for the two types of fluorapatite will be discusses separately below.

The presence of halite-bearing fluid inclusions (Fig. 8h and 8i) in the altered zones of disseminated fluorapatite indicates that the metasomatic fluids were highly saline (i.e. high in Cl and Na). Indeed, previous fluid reaction experiments have shown that fluorapatite tends to be easily altered in Cl-rich fluids (e.g., Harlov and Forster 2003; Harlov et al. 2005). Recent studies have demonstrated that chloride ions can form stable complex with REEs, especially in fluids with high temperatures and low pH (Migdisov and Williams-Jones 2006; Migdisov et al. 2009). Thus, REEs could have been effectively leached out of the fluorapatite by such Cl-rich fluids. It is notable that Cl preferentially combines with LREE at elevated temperatures, resulting in decoupling of LREEs and HREEs (e.g., Wood 1990; Migdisov et al. 2009). However, the altered disseminated fluorapatite shows similar degrees of removal of LREE (La to Eu) and HREE (Gd to Lu) (Fig. 11a). Therefore, other ligands that tend to combine with HREE, such as F, must also have been present in the fluids. Allanite inclusions are present in the altered domains of disseminated fluorapatite. Previous studies have

Always consult and cite the final, published document. See http:/www.minsocam.org or GeoscienceWorld

518 suggested that high Ca activities destabilize monazite and promote the formation of
519 REE-epidote and allanite when F is present in the fluids (e.g., Rasmussen and
520 Muhling 2009; Budzyń et al. 2011). It has been experimentally demonstrated that the
521 presence of Ca and Na in metasomatic fluids can suppress the growth of REE mineral
522 phases in altered apatite (Harlov and Förster 2003). This could explain why REE
523 mineral inclusions are sparse in the altered zones of disseminated fluorapatite (Fig.
524 8a-8f), even if a large portion of the REE was released during metasomatic alteration
525 (Fig. 11a). In general, the fluids responsible for the alteration of disseminated
526 fluorapatite were rich in Cl and Na, and also contained F and Ca.

527 Anhydrites are common in the altered zones of the Taocun vein fluorapatite (Fig.
528 9f and 9h), implying that SO_4^{2-} would have been an important ligand in the
529 metasomatic fluids. The occurrence of calcite inclusions in the altered domains (Fig.
530 9d and 9h) indicates that the fluids may have contained CO_3^{2-} as well. The altered
531 vein fluorapatites show lower degrees of total REE removal, and compared to
532 disseminated fluorapatite only LREE are removed (Fig. 11), suggesting that Cl was an
533 important component in the fluids. Considering that both SO_4^{2-} and CO_3^{2-} are also
534 effective in enhancing REE transportation and mobility (e.g., Hass et al. 1995), the
535 depletion of LREE (Fig. 11b) in altered vein fluorapatite indicates that the
536 metasomatic fluids may have had high concentrations of REEs, in other words be
537 close to REE saturation. Allanite and anhydrite occur as inclusions in both interstitial
538 and vein fluorapatite crystals and occur as a fracture-filling phase (Fig. 9e, 9g and 9i),
539 suggesting Ca^{2+} may also have been abundant in the metasomatic fluids. In summary,
540 we propose that the metasomatic fluids were enriched in SO_4^{2-} and Ca^{2+}, but also
541 contained lesser amounts of Cl^- and CO_3^{2-}.

542 **Timing of metasomatic alteration of the fluorapatite**

543 Analyses of the unaltered vein fluorapatite yielded a consistent weighted mean
544 $^{206}Pb/^{238}U$ age of 131.1 ± 1.9 Ma and an intercept age of 131.1 ± 1.9 Ma (Fig. 14),
545 both of which are almost identical to the zircon U-Pb age of 130.7 ± 1.8 Ma obtained
546 from the diorite intrusion (Fan et al. 2010; Zhou et al. 2013). These data show that the
547 ore mineralization was related to the emplacement of the subvolcanic diorite intrusion.

Always consult and cite the final, published document. See http:/www.minsocam.org or GeoscienceWorld

548 Because vein-type ores structurally crosscut disseminated ores, the ages of unaltered
549 vein fluorapatite provide a lowest estimate of the age of ore formation. In the
550 Tera-Wasserburg plots of $^{238}U/^{206}Pb$ vs. $^{207}Pb/^{206}Pb$, altered fluorapatite plot on a
551 linear extension of the unaltered grains (Fig. 14a), implying that the metasomatic
552 alteration took placed shortly after formation of the mineral, an age difference too
553 small to be distinguished using U-Pb isotopic dating.

554 It should be noted that the Ningwu volcanic basin has not undergone any regional
555 metamorphism or basin inversion after its formation in the early Cretaceous (e.g.,
556 Ningwu Research Group 1978; Xu 1990; Pan and Dong 1999). The altered
557 fluorapatite has fluid inclusions with homogenization temperatures as high as 400 °C
558 (Ma et al. 2006) that also contain salt minerals. Such high temperatures and highly
559 saline fluids were most likely magmatic-hydrothermal in origin that developed during
560 the later stage of ore-formation, a conclusion also consistent with the U-Pb dating of
561 the fluorapatite.

562 We emphasize that metasomatic alteration of fluorapatite is a common
563 phenomenon in IOA deposits (e.g., Harlov et al. 2002; Torab and Lehmann 2007;
564 Bonyadi et al. 2011 ; Stosch et al. 2011). U-Pb dating and geological relationships
565 suggest that fluorapatite in the Taocun deposit underwent metasomatic alteration
566 shortly after precipitation of the original mineral.

567 **Possible origin of ore fluids and metasomatic fluids**

568 The unaltered fluorapatite grains have $\delta^{18}O$ values ranging from +5.3 to +7.5 ‰
569 (Fig. 13; Table 2), which are consistent with zircon $\delta^{18}O$ values ranging from +5.4 to
570 +6.8 ‰ from the dioritic intrusions in the region (Yan et al. 2015). They have initial
571 $^{87}Sr/^{86}Sr$ ratios of 0.70777 to 0.70868 (Fig. 12; Table 1), which are only slightly
572 higher than the ore-hosting intrusions and volcanic rocks with initial $^{87}Sr/^{86}Sr$ ratios
573 ranging from 0.7055 to 0.7077 (e.g., Ishihara et al. 1986; Tang et al. 1998; Hou et al.
574 2012). In the Ningwu Basin, volcanic rocks were underlain by Triassic carbonate
575 sequences and Jurassic clastic sedimentary rocks (e.g., Ningwu Research Group 1978;
576 Xu 1990; Pan and Dong 1999). These sedimentary rocks have $^{87}Sr/^{86}Sr_i$ ratios of

Always consult and cite the final, published document. See http:/www.minsocam.org or GeoscienceWorld

577 0.7138 to 0.7151 (Wang 2011), much higher than those of ore fluorapatite, and
578 provide a plausible source for radiogenic Sr. The slight increase of $^{87}Sr/^{86}Sr$ ratios in
579 the ore fluorapatite was likely due to interaction between the ore fluids and
580 sedimentary rocks. The Sr and O isotopic compositions of ore fluorapatite thus imply
581 that the early-stage, ore-forming fluids were magmatic in origin but underwent weak
582 interaction with the country rocks.

583 In both the disseminated and vein fluorapatite in the Taocun deposit, there is
584 apparent increases in $^{87}Sr/^{86}Sr$ ratios from unaltered to altered domains (Fig. 12). Such
585 variations indicate that the metasomatic fluids were more enriched in radiogenic Sr
586 and likely had a greater contribution from the sedimentary rocks due to fluid
587 circulation (Fig. 15a and 15b). On the other hand, the altered domains of ore
588 fluorapatite have a large range of $\delta^{18}O$ values as low as -3.0 ‰ (Fig. 13), indicating
589 that the metasomatic fluids were low in $\delta^{18}O$. The shift to lighter oxygen isotopes of
590 the metasomatic fluids can be due to either fluid-wallrock interaction or the addition
591 of ^{18}O-depleted fluids. Carbonate rocks in the sedimentary sequence in Ningwu basin
592 have particularly high $\delta^{18}O$ values with an average of 25.5 ‰ (Hou et al. 2004). Thus,
593 local fluid-wallrock interaction cannot lead to an ^{18}O-depleted signature of the fluids.
594 Alternatively, the addition of $\delta^{18}O$-depleted fluids, such as meteoric water, could have
595 significantly lowered the oxygen isotopic compositions of the metasomatic fluids.
596 However, fluid inclusions in the altered fluorapatite contain halite and have
597 homogenization temperature up to 400 °C, precluding a single source of meteoric
598 water. Therefore, we propose that meteoric water mixed with earlier magmatic fluids
599 and then interacted with the country rocks (Fig. 15a and 15b). The combination of
600 these processes could account for the late-stage fluids with low $\delta^{18}O$ but high
601 radiogenic Sr. In summary, primary fluorapatite grains of both types of ores were
602 precipitated from high-temperature magmatic fluids. These fluids were subsequently
603 mixed with meteoric water at stage III and stage iii, in which
604 dissolution-reprecipitation processes occurred in the fluorapatite (Fig. 15c and 15d).
605 The incorporated meteoric water may have interacted with different strata during fluid
606 circulation, so the two types of metasomatic fluids show somewhat different

Always consult and cite the final, published document. See http:/www.minsocam.org or GeoscienceWorld

607 characteristics.

608

609 **IMPLICATIONS**

610 Elemental and isotopic compositions of apatite are commonly utilized to obtain a
611 record of magmatic and hydrothermal events (e.g., Belousova et al. 2002; Piccoli and
612 Candela 2002; Harlov 2015; Kusebauch et al. 2015; Webster and Piccoli 2015).
613 However, recent studies have revealed that apatite commonly undergoes significant
614 fluid metasomatism, resulting in significant modification of its elemental composition.
615 In many IOA deposits altered fluorapatites are generally characterized by much lower
616 REEs, Si, and Na than the unaltered grains, and they also show decreased S, Cl, and
617 other bivalent atoms (Mg, Mn, Fe, and Sr) (e.g., Harlov et al. 2002; Harlov and
618 Förster 2003; Harlov et al. 2005; Torab and Lehmann 2007; Li and Zhou 2015).
619 However, little attention has been paid to the effects of alteration on the stable and
620 radiogenic isotopes of fluorapatite in hydrothermal ore deposits (e.g., Stosch et al.
621 2011; Li and Zhou 2015; Zhao et al. 2015).

622 In this study, an integrated analysis of *in situ* elemental and isotopic (U-Pb, Sr, and
623 O) compositions, for the first time, demonstrates that hydrothermal alteration can not
624 only significantly modify trace elements, but also Sr and O isotopes of fluorapatite
625 during a later stage of an ore-forming event. The Sr and O isotope values of the
626 primary fluorapatite are significantly different from the altered grains/domains (Figs.
627 12 and 13). The $\delta^{18}O$ values between the primary and altered fluorapatite have the
628 greatest variation up to ~10 ‰. As addressed above, $\delta^{18}O$ values of the primary
629 fluorapatite reflect the dominance of magmatic fluids, whereas the altered fluorapatite
630 clearly show contributions of meteoric water to the metasomatic fluids. In contrast,
631 bulk O isotopic data of fluorapatite separates show a mixture of O isotopic signatures
632 (Fig. 13), and are therefore geologically misleading. However, oxygen isotope
633 analysis of bulk minerals is an important tool widely adopted in the study of
634 hydrothermal systems (e.g., Zheng 1996; Chen 2008; Nabatian and Ghaderi 2013; Yu
635 et al. 2015). It is expected that, if metasomatism occurs, fluorapatite with mixed
636 isotopic signatures may give a misleading interpretation of fluid sources. This study

Always consult and cite the final, published document. See http:/www.minsocam.org or GeoscienceWorld

637 has also shown that metasomatic alteration of fluorapatite can occur during a late
638 stage of the ore-forming event, when early ore fluids had been modified by fluid
639 mixing, cooling, and interaction with country rocks. Therefore, it is important to
640 evaluate such processes on mineral textures and chemistry before using apatite as an
641 indicator mineral when studying IOA and other hydrothermal ore deposits.
642

643 **ACKNOWLEDGEMENTS**

644 This study was supported by the 973 program (2012CB416802) and the Fundamental
645 Research Funds for the Central Universities (CUG140618). We thank the local
646 geologists, Minlin Rui and Zhangyan Shi, for their assistance in the field, Meijun
647 Yang for the EMPA analyses, Congying Li for the LA-ICPMS analyses, Tao Yang for
648 the LA-MC-ICPMS analyses, Xian-Hua Li and Xiaoxiao Lin for the SIMS O isotope
649 analyses, and Rick Moscati for the bulk mineral oxygen isotopic analyses at the
650 USGS. We appreciate Prof. Paul Robinson for polishing the English. We are grateful
651 to Prof. David Lentz and an anonymous reviewer for their constructive comments,
652 and Prof. Daniel Harlov for handling the manuscript.
653

654 **REFERENCES CITED**

655 Anhui Bureau of Geology. (1975) The Geological Characteristics, Metallogenic
656 Condition and Prospecting Targets of the Iron Deposits in Ma'anshan District,
657 Middle Part of Ningwu Basin., 61 pp. Unpublished Report (in Chinese).
658 Armstrong, J.T. (1991) Quantitative elemental analysis of individual microparticles
659 with electron beam instruments. In K.F.J. Heinrich, and D. Newbury, Eds.,
660 Electron Probe Quantitation, p. 261-345. Plenum Press, New York.
661 Belousova, E.A., Griffin, W.L., O'Reilly, S.Y., and Fisher, N.I. (2002) Apatite as an
662 indicator mineral for mineral exploration: trace-element compositions and their
663 relationship to host rock type. Journal of Geochemical Exploration, 76, 45-69.
664 Bonyadi, Z., Davidson, G.J., Mehrabi, B., Meffre, S., and Ghazban, F. (2011)
665 Significance of apatite REE depletion and monazite inclusions in the brecciated
666 Se-Chahun iron oxide-apatite deposit, Bafq district, Iran: Insights from
667 paragenesis and geochemistry. Chemical Geology, 281, 253-269.
668 Budzyń, B., Harlov, D.E., Williams, M.L., and Jercinovic, M.J. (2011) Experimental
669 determination of stability relations between monazite, fluorapatite, allanite, and
670 REE-epidote as a function of pressure, temperature, and fluid composition.
671 American Mineralogist, 96, 1547-1567.
672 Chen, H.Y. (2008) The Marcona-Mina Justa district, south-central Peru: Implications

Always consult and cite the final, published document. See http:/www.minsocam.org or GeoscienceWorld

673 for the genesis and definition of the Iron Oxide-Copper (-Gold) ore deposit clan,
674 266 pp. Ph.D. thesis, Queen's University, Kingston.
675 Chen, W.T., and Zhou, M.F. (2015) Mineralogical and geochemical constraints on
676 mobilization and mineralization of rare Earth elements in the Lala Fe-Cu-(Mo,
677 Ree) deposit, SW China. American Journal of Science, 315, 671-711.
678 Chew, D.M., Sylvester, P.J., and Tubrett, M.N. (2011) U-Pb and Th-Pb dating of
679 apatite by LA-ICPMS. Chemical Geology, 280, 200-216.
680 Clayton, R.N., and Mayeda, T.K. (1963) The use of bromine pentafluoride in the
681 extraction of oxygen from oxides and silicates for isotopic analysis. Geochimica et
682 Cosmochimica Acta, 27, 43-52.
683 Duan, C., Mao, J.W., Li, Y.H., Hou, K.J., Yuan, S.D., Zhang, C., and Liu, J.L.(2011)
684 Zircon U-Pb geochronology of the gabbro-diorite porphyry and granodiorite
685 porphyry from the Washan iron deposit in Ningwu Basin, and its geological
686 significance. Acta Geologica Sinica, 85, 1159-1171(in Chinese).
687 Fan, Y., Zhou, T.F., Yuan, F., Zhang, L.J., Qian, B., Ma, C.Q., and David, R.C. (2010)
688 Geochronology of the diorite porphyrites in the Ning-Wu Basin and their
689 metallogenic significances. Acta Petrologica Sinica, 26, 2715-2728(in Chinese).
690 Frietsch, R., and Perdahl, J.-A. (1995) Rare earth elements in apatite and magnetite in
691 Kiruna-type iron ores and some other iron ore types. Ore Geology Reviews, 9,
692 489-510.
693 Gao, J.F., and Zhou, M.F. (2013) Generation and evolution of siliceous high
694 magnesium basaltic magmas in the formation of the Permian Huangshandong
695 intrusion (Xinjiang, NW China). Lithos, 162-163, 128-139.
696 Haas, J.R., Shock, E.L., and Sassani, D.C. (1995) Rare earth elements in hydrothermal
697 systems: Estimates of standard partial molal thermodynamic properties of aqueous
698 complexes of the rare earth elements at high pressures and temperatures.
699 Geochimica et Cosmochimica Acta, 59, 4329-4350.
700 Harlov, D.E. (2015) Apatite: A fingerprint for metasomatic processes. Elements, 11,
701 171-176.
702 Harlov, D.E., Andersson, U.B., Förster, H.-J., Nyström, J.O., Dulski, P., and Broman,
703 C. (2002) Apatite-monazite relations in the Kiirunavaara magnetite-apatite ore,
704 northern Sweden. Chemical Geology, 191, 47-72.
705 Harlov, D.E., and Förster, H.-J. (2003) Fluid-induced nucleation of
706 (Y+REE)-phosphate minerals within apatite: Nature and experiment. Part II.
707 Fluorapatite. American Mineralogist, 88, 1209-1229.
708 Harlov, D.E., Wirth, R., and Förster, H. (2005) An experimental study of
709 dissolution-reprecipitation in fluorapatite: fluid infiltration and the formation of
710 monazite. Contributions to Mineralogy and Petrology, 150, 268-286.
711 Hou, K.J., and Yuan, S.D. (2010) LA-ICP-MS zircon U-Pb dating and Hf component
712 of the magmatic rocks in Ningwu Cretaceous volcanic basin in Anhui Province
713 and its geological significance. Acta Geologica Sinica, 26, 888-902 (in Chinese).
714 Hou, T., Zhang, Z.C., Encarnacion, J., Huang, H., and Meng, W. (2012)
715 Geochronology/geochemistry of the Washan dioritic porphyry associated with
716 Kiruna-type iron ores, Middle-Lower Yangtze River Valley, eastern China:

Always consult and cite the final, published document. See http:/www.minsocam.org or GeoscienceWorld

implications for petrogenesis/mineralization. International Geology Review, 54, 1332-1352.

Hou, Z.Q., Yang, Z.S., Li, Y.Q., Zeng, P.S., Meng, Y.F., Xu, W.Y., and Tian, S.H. (2004) Large-scale migration of fluids towards foreland basins during collisional orogeny: Evidence from Triassic anhydrock sequences and regional alteration in Middle-Lower Yangtze area. Mineral Deposits, 23, 310-326 (in Chinese).

Ishihara, S., Li, W.D., Sasaki, A., Shibata, K., Matsuhisa, Y., and Terashima, S. (1986) Characteristics of Cretaceous magmatism and related mineralization of the Ningwu basin, Lower Yangtze area, eastern China. Bulletin of the Geological Survey of Japan, 37, 207-231.

Jami, M., Dunlop, A.C., and Cohen, D.R. (2007) Fluid inclusion and stable isotope study of the Esfordi apatite-magnetite deposit, Central Iran. Economic Geology, 102, 1111-1128.

Kusebauch, C., John, T., Whitehouse, M.J., and Engvik, A.K. (2015) Apatite as probe for the halogen composition of metamorphic fluids (Bamble Sector, SE Norway). Contributions to Mineralogy and Petrology, 170, 1-20.

Li, X.H., Li, W.X., Li, Q.L., Wang, X.C., Liu, Y., and Yang, Y.H. (2010) Petrogenesis and tectonic significance of the ~850 Ma Gangbian alkaline complex in South China: Evidence from in situ zircon U-Pb dating, Hf-O isotopes and whole-rock geochemistry. Lithos, 114, 1-15.

Li, X.C., Zhao, X.F., Zhou, M.F., Chen, W.T., and Chu, Z.Y. (2015) Fluid inclusion and isotopic constraints on the origin of the Paleoproterozoic Yinachang Fe-Cu-(REE) Deposit, Southwest China. Economic Geology, 110, 1339-1369.

Li, X.C., and Zhou, M.F. (2015) Multiple stages of hydrothermal REE remobilization recorded in fluorapatite in the Paleoproterozoic Yinachang Fe-Cu-(REE) deposit, Southwest China. Geochimica et Cosmochimica Acta, 166, 53-73.

Liu, Y.S., Hu, Z.C., Gao, S., Günther, D., Xu, J., Gao, C.G., and Chen, H.H. (2008) In situ analysis of major and trace elements of anhydrous minerals by LA-ICP-MS without applying an internal standard. Chemical Geology, 257, 34-43.

Ludwig, K.R. (2003) User's Manual for Isoplot 3.00: a Geochronological Toolkit for Microsoft Excel. Berkeley Geochronology Center, Berkeley.

Ma, F., Jiang, S.Y., Jiang, Y.H., Ni, P., and Ling, H.F. (2006) Fluid inclusions and H-O isotopic compositions in the Washan and Dongshan iron deposits,Ningwu basin,China. Acta Petrologica Sinica, 22, 2581-2589 (in Chinese).

Mao, J.W., Xie, G.Q., Duan, C., Pirajno, F., Ishiyama, D., and Chen, Y.C. (2011) A tectono-genetic model for porphyry-skarn-stratabound Cu-Au-Mo-Fe and magnetite-apatite deposits along the Middle-Lower Yangtze River Valley, Eastern China. Ore Geology Reviews, 43, 294-314.

Masteel Mining Co. Ltd. (2012) The Secondary Stage Exploration Report of Resource Reserves of the Gaocun Iron Deposit, Ma'anshan City, Anhui Province, 26 p. Unpublished Report (in Chinese).

Migdisov, A.A., and Williams-Jones, A.E. (2006) A spectrophotometric study of erbium (III) speciation in chloride solutions at elevated temperatures. Chemical Geology, 234, 17-27.

Always consult and cite the final, published document. See http:/www.minsocam.org or GeoscienceWorld

Migdisov, A.A., Williams-Jones, A.E., and Wagner, T. (2009) An experimental study of the solubility and speciation of the Rare Earth Elements (III) in fluoride- and chloride-bearing aqueous solutions at temperatures up to 300 °C. Geochimica et Cosmochimica Acta, 73, 7087-7109.

Nabatian, G., and Ghaderi, M. (2013) Oxygen isotope and fluid inclusion study of the Sorkhe-Dizaj iron oxide-apatite deposit, NW Iran. International Geology Review, 55, 397-410.

Ningwu Research Group. (1978) Ningwu Porphyry Iron Ores, 196 pp. Geological Publishing House, Beijing (in Chinese).

Pan, Y.M., and Dong P. (1999) Lower Changjiang (Yangzir/Yangtze River) metallogenic belt, east central China: intrusion and wall rock-hosted Cu-Fe-Au, Mo, Zn, Pb, Ag deposits. Ore Geology Reviews, 15, 177-242.

Pan, Y.M., and Fleet, M.E. (2002) Compositions of the apatite-group minerals: substitution mechanisms and controlling factors. Reviews in Mineralogy and Geochemistry, 48, 13-49.

Paton, C., Hellstrom, J., Paul, B., Woodhead, J., and Hergt, J. (2011) Iolite: Freeware for the visualisation and processing of mass spectrometric data. Journal of Analytical Atomic Spectrometry, 26, 2508-2518.

Petrus, J.A., and Kamber, B.S. (2012) VizualAge: A Novel Approach to Laser Ablation ICP-MS U-Pb Geochronology Data Reduction. Geostandards and Geoanalytical Research, 36, 247-270.

Piccoli, P.M., and Candela, P.A. (2002) Apatite in Igneous Systems. Reviews in Mineralogy and Geochemistry, 48, 255-292.

Putnis, A. (2002) Mineral replacement reactions: from macroscopic observations to microscopic mechanisms. Mineralogical Magazine, 66, 689-708.

——— (2009) Mineral Replacement Reactions. Reviews in Mineralogy and Geochemistry, 70, 87-124.

Ramos, F.C., Wolff, J.A., and Tollstrup, D.L. (2004) Measuring $^{87}Sr/^{86}Sr$ variations in minerals and groundmass from basalts using LA-MC-ICPMS. Chemical Geology, 211, 135-158.

Rasmussena, B., and Muhling, J.R. (2009) Reactions destroying detrital monazite in greenschist-facies sandstones from the Witwatersrand basin, South Africa. Chemical Geology, 264, 311-327.

Stosch, H., Romer, R.L., Daliran, F., and Rhede, D. (2011) Uranium-lead ages of apatite from iron oxide ores of the Bafq District, East-Central Iran. Mineralium Deposita, 46, 9-21.

Sun, S.S., and McDonough, W.F. (1989) Chemical and isotopic systematics of oceanic basalts: implications for mantle composition and processes. Geological Society, London, Special Publications, 42, 313-345.

Tang, Y.C., Wu, Y.C., Chu, G.Z., Xing, F.M., Wang, Y.M., Gao, F.Y., and Chang, Y.F. (1998) Geology of Copper-gold Polymetallic Deposits in the Along Changjiang Area of Anhui Province, 351 pp. Geological Publishing House, Beijing (in Chinese).

Thomson, S.N., Gehrels, G.E., Ruiz, J., and Buchwaldt, R. (2012) Routine

Always consult and cite the final, published document. See http:/www.minsocam.org or GeoscienceWorld

low-damage apatite U-Pb dating using laser ablation-multicollector-ICPMS. Geochemistry, Geophysics, Geosystems, 13, 1525-2027.

Torab, F.M., and Lehmann, B. (2007) Magnetite-apatite deposits of the Bafq district, Central Iran: apatite geochemistry and monazite geochronology. Mineralogical Magazine, 71, 347-363.

Tu, X.L., Zhang, H., Deng, W.F., Ling, M.X., Liang, H.Y., Liu, Y., and Sun, W.D. (2011) Application of RESOlution in-situ laser ablation ICP-MS in trace element analyses. Geochimica, 40, 83-98 (in Chinese).

Vroon, P.Z., Van, Der Wagt B., Koornneef, J.M., and Davies, G.R. (2008) Problems in obtaining precise and accurate Sr isotope analysis from geological materials using laser ablation MC-ICPMS. Analytical and Bioanalytical Chemistry, 390, 465-476.

Wang, W.C.(2011) Effect of sulfate evaporate salt layer for formation of the Nihe iron deposit in the Luzong basin, China, 78 pp. M.D. thesis, HeFei University of Technology., He Fei (in Chinese).

Webster, J.D., and Piccoli, P.M. (2015) Magmatic apatite: A powerful, yet deceptive, mineral. Elements, 11, 177-182.

Wood, S.A. (1990) The aqueous geochemistry of the rare-earth elements and yttrium: 2. Theoretical predictions of speciation in hydrothermal solutions to 350°C at saturation water vapor pressure. Chemical Geology, 88, 99-125.

Wu, F.Y., Yang, Y.H., Marks, M.A.W., Liu, Z.C., Zhou, Q., Ge, W.C., Yang, J.S., Zhao, Z.F., Mitchell, R.H., and Markl, G. (2010) In situ U-Pb, Sr, Nd and Hf isotopic analysis of eudialyte by LA-(MC)-ICP-MS. Chemical Geology, 273, 8-34.

Xing, F.M. (1996) Petrological and Nd, Sr, Pb isotopic evidence for genesis of Mesozoic magmatic rocks in Nanjing-Wuhu area. Acta Petrologica Et Mineralogica, 15, 126-137 (in Chinese).

Xu, Z.G. (1990) Mesozoic volcanism and volcanogenic iron-ore deposits in eastern China. Geological Society of America Special Papers, 237, 1-49.

Yan, J., Liu, J.M., Li, Q.Z, Xing, G.F., Liu, X.Q., Xie, J.C., Chu, X.Q., and Chen, Z.H. (2015) In situ zircon Hf-O isotopic analyses of late Mesozoic magmatic rocks in the Lower Yangtze River Belt, central eastern China: Implications for petrogenesis and geodynamic evolution. Lithos, 227, 57-76.

Yang, Y.H., Wu, F.Y., Wilde, S.A., Liu, X.M., Zhang, Y.B., Xie, L.W., and Yang, J.H. (2009a) In situ perovskite Sr-Nd isotopic constraints on the petrogenesis of the Ordovician Mengyin kimberlites in the North China Craton. Chemical Geology, 264, 24-42.

Yang, Y.H., Wu, F.Y., Xie, L.W., Yang, J.H., and Zhang, Y.B. (2009b) In-situ Sr isotopic measurement of natural geological samples by LA-MC-ICP-MS. Acta Petrologica Sinica, 25, 3431-3441 (in Chinese).

Yu, J.J., Che, L.R., and Wang, T.Z. (2015) Alteration, oxygen isotope, and fluid inclusion study of the Meishan iron oxide-apatite deposit, SE China. Mineralium Deposita, 50, 847-869.

Yuan, F., Zhou, T.F., Fan, Y., Zhang, L.J., Ma, L., and Qian, B. (2011) Zircon U-Pb

Always consult and cite the final, published document. See http:/www.minsocam.org or GeoscienceWorld

ages and isotopic characteristics of the granitoids in the Ningwu basin, China. Acta Geologica Sinica, 85, 821-833 (in Chinese).

Yuan, S.D., Hou, K.J., and Liu, M. (2010) Timing of mineralization and geodynamic framework of iron-oxide-apatite deposits in Ningwu Cretaceous basin in the Middle-Lower Reaches of the Yangtze River,China: Constraints from Ar-Ar dating on phlogopites. Acta Petrologica Sinica. 26, 797-808 (in Chinese).

Zhai, Y.S., Yao, S.Z., Lin, X.D., Zhou, X.N., Wan, T.F., Jin, F.Q., and Zhou, Z.G. (1992) Fe-Cu(Au) Metallogeny of the Middle-Lower Changjiang Region, 235 pp. Geological Publishing House, Beijing (in Chinese).

Zhang, Q., Jian, P., Liu, D.Y., Wang, Y.L., Qian, Q., Wang, Y., and Xue, H. (2003) SHRIMP dating of volcanic rocks from Ningwu area and geological implication. Science in China (series D), 33, 309-314 (in Chinese).

Zhao, X.F., Zhou, M.F., Gao, J.F., Li, X.C., and Li, J.W. (2015) In situ Sr isotope analysis of apatite by LA-MC-ICPMS: constraints on the evolution of ore fluids of the Yinachang Fe-Cu-REE deposit, Southwest China. Mineralium Deposita, 50, 871-884.

Zheng, Y.F. (1996) Oxygen isotope fractionations involving apatites: Application to paleotemperature determination. Chemical Geology, 127, 177-187.

Zhou, T.F., Yu, F., Feng, Y., Zhang, L.J., Qian, B., Ma, L., Yang, X.F., and David, R.C. (2011) Geochronology and significance of volcanic rocks in the Ning-Wu of China. Science China Earth Sciences, 54, 185-196 (in Chinese).

Zhou, T.F., Fan, Y., Yuan, F., Zhang, L.J., Qian, B., Ma, L., and Yang, X.F. (2013) Geology and geochronology of magnetite-apatite deposits in the Ning-Wu volcanic basin, eastern China. Journal of Asian Earth Sciences, 66, 90-107.

List of Figure Caption:

FIGURE 1. (**a**) Tectonic division of South China showing the location of the Middle-Lower Yangtze River Valley metallogenic belt (MLYRVMB). (**b**) Tectonic map showing the distribution of IOA deposits, and related early Cretaceous volcanic basins along the MLYRVMB (modified from Mao et al. 2011).

TLF: Tancheng-Lujiang Fault; XGF: Xiangfan-Guangji Fault; YCF: Yangxing-Changzhou Fault.

FIGURE 2. Simplified geological map of Ningwu volcanic basin showing the volcanic sequences, sub-volcanic intrusions, and distribution of IOA deposits (after Ningwu Research Group 1978).

FIGURE 3. Simplified geological map of the Taocun IOA deposit. Note that the bodies are located in the apical zone of the ore-hosting intrusion (modified from

Always consult and cite the final, published document. See http:/www.minsocam.org or GeoscienceWorld

888 Masteel Mining Co. Ltd. 2012).

889 **FIGURE 4.** Cross section of No.4 exploration line of the Taocun IOA deposit
890 showing the spatial association between the iron ore deposit and alteration halos
891 (modified from Anhui Bureau of Geology 1975). Note that the orebodies are located
892 within the intermediate alteration zone with extensive actinolite, albite, apatite,
893 chlorite, and epidote.

894 **FIGURE 5.** Photos of representative disseminated and vein-type ores showing typical
895 ore textures and hydrothermal alteration. (**a**) Densely disseminated magnetite is in
896 intimate association with euhedral pseudomorphic scapolite, marking the latest stage
897 of stage I sodic alteration and the beginning of magnetite precipitation. (**b**) Polished
898 slab of disseminated ore consisting of intergrown magnetite (black) and albite (grey),
899 which were locally overprinted by late stage interstitial epidote (green). (**c**) Polished
900 slab of typical vein-type ore with associated pegmatitic apatite, magnetite, and
901 actinolite, which was locally overprinted by later pyrite. (**d**) The albitized diorite
902 intrusion was crosscut by a coarse-grained magnetite-actinolite vein, indicating
903 vein-type ores were slightly later than the main orebody. Note that the
904 magnetite-actinolite veins are enveloped by alteration halos of albite and epidote. (**e**)
905 Disseminated ore crosscut by a magnetite-actinolite vein, and both are crosscut by
906 late-stage, fracture-filling quartz veinlets. Note that the contacts between the
907 disseminated ore and magnetite-actinolite vein have brown alteration halos (likely
908 albite). (**f**) Coarse-grained magnetite-actinolite vein crosscut by greyish anhydrite
909 veins, which are, in turn, cut by later calcite veinlets.

910 Mineral abbreviations: Ab-albite; Act-actinolite; Anh-anhydrite; Ap-apatite;
911 Cal-calcite; Mag-magnetite; Py-pyrite; Qz-quartz; Scp-scapolite.

912 **FIGURE 6.** (**a**) High contrast BSE image of disseminated ore showing that euhedral
913 fluorapatite is closely associated with magnetite and albite, note rims of apatite grains
914 are partially metasomatized; (**b**) BSE image showing that euhedral to subhedral
915 fluorapatite grains in disseminated ore are extensively metasomatized. Note that the
916 altered domains contain fine-grained allanite and albite inclusions. (**c**) and (d)
917 Euhedral vein fluorapatite is intergrown with magnetite and actinolite. Note that the

Always consult and cite the final, published document. See http:/www.minsocam.org or GeoscienceWorld

fluorapatite is partially metasomatized along fractures, and fine-grained allanite occurs along the fractures or is interstitial to the crystals.

Abbreviations: Aln-allanite. Other abbreviations are the same as those in Fig. 5.

FIGURE 7. Paragenetic sequence of mineralization and alteration minerals in the Taocun IOA deposit. Note the dashed line between the disseminated and vein-type mineralization. The stage IV of disseminated mineralization likely postdates stages i and ii of vein-type mineralization

FIGURE 8. BSE images (**a-f**) showing metasomatic textures of disseminated fluorapatite in the Taocun deposit, and photomicrographs of fluid inclusions within fluorapatite (**g-i**). Note that many of the fluorapatite grains show irregular patchy zones and host minor REE-bearing minerals. (**a**) Unaltered fluorapatite has oscillatory zoning under BSE imaging, and was metasomatically altered by fluid at the rim as shown by the many voids and mineral inclusions. (**b**) Metasomatically altered fluorapatite grain containing sparse allanite inclusions in the altered domain. (**c**) and (**d**) Almost completely replaced grain has numerous voids and mineral inclusions of allanite and albite. Note the intimate association of allanite and albite inclusions implying they are co-genetic alteration products. (**e**) The inner domain of fresh fluorapatite has a sharp contact with the altered domain of irregular patches. Note the altered fluorapatite zone contains sparse monazite inclusions. (**f**) Monazite inclusions show a preferred orientation parallel to the c-axis of fluorapatite. (**g**) Transmitted microscopic photos of a fluorapatite grain showing that fluid inclusions within unaltered and altered domains are significantly different. Needle-shaped fluid inclusions occur in the unaltered zone parallel to the crystallographic c-axis of the host mineral, but there is no preferred orientation for fluid inclusions in altered rims. (**h**) Coexistence of different types of fluid inclusions in the altered fluorapatite: three-phases (L+V+S), two-phases (L +V), and mono-phase (V, L). The transparent daughter crystal is halite. (**i**) A representative fluid inclusion containing two solid phases; one is halite, and the other is an unknown phase.

Abbreviations: Mnz-monazite; L-aqueous phase; S-solid phase; V-vapor phase. Other abbreviations are the same as those in Figs. 5 and 6.

Always consult and cite the final, published document. See http:/www.minsocam.org or GeoscienceWorld

948 **FIGURE 9.** Transmitted, microscopic CL and BSE photomicrographs of
949 representative vein fluorapatite. (**a**) Transmitted photomicrograph and (**b**) microscopic
950 CL image of a pegmatitic fluorapatite crystal showing that its metasomatic texture can
951 be easily identified in microscopic CL imaging; the fresh domain is blue and the
952 altered domain is yellow-greenish. (**c**) and (**d**) BSE images of a section of (**b)** showing
953 that the altered regions are darker and have many voids and mineral inclusions. (**e**)
954 and (**f**) BSE images showing that the altered vein fluorapatite contains some mineral
955 inclusions of anhydrite and monazite, which are crosscut by a stage iv calcite vein.
956 Note also that allanite occurs within the fractures of the crystal. (**g**) and (**h**) Altered
957 fluoapatite grain has inclusions of monazite, anhydrite, and calcite, whereas allanite
958 occurs within fractures. (**i**) BSE image showing that fluid metasomatism is more
959 extensive at the rims of fluorapatite. Quartz, calcite and allanite are mostly interstitial
960 to fluorapatite.
961 Abbreviations are the same as those in Figs. 5-6 and 8.
962 **FIGURE 10.** (**a**) Plots of S (apfu) vs. Na (apfu) showing a positive correlation
963 between S and Na for both types of fluorapatite. Note the altered zones/grains of both
964 types contain much lower S and Na than the unaltered grains. Plots of Si vs. total
965 REE+Y (**b**), La_N/Yb_N ratios vs. total REE+Y (**c**), Th vs. U (**d**), Sr vs. Mg (**e**), and V vs.
966 Fe (**f**) based on LA-ICPMS analysis of altered and fresh grains from the two types of
967 fluorapatite. Note the altered grains/zones of both types have elemental compositions
968 significantly lower than the unaltered grains.
969 **FIGURE 11.** Chondrite-normalized rare earth element patterns of (**a**) disseminated
970 and (**b**) vein fluorapatite. Note that both fluorapatite types release REEs during fluid
971 alteration. However, both LREE and HREE were lost from disseminated fluorapatite,
972 whereas only LREE were obviously removed from vein fluorapatite. Chondrite values
973 used for normalization are from Sun and McDonough (1989).
974 **FIGURE 12.** Plot of *in-situ* $^{87}Sr/^{86}Sr$ ratios vs. ^{88}Sr (v)' values of the altered and fresh
975 grains from the two types of fluorapatite in the Taocun deposit. Because different
976 repetition pulse rate can influence the ^{88}Sr ion signal intensity (Vroon et al. 2008), ^{88}Sr
977 (v) was normalized to repetition pulse rate (Hz) of each analysis, and then magnified

Always consult and cite the final, published document. See http:/www.minsocam.org or GeoscienceWorld

by eight times, namely ^{88}Sr (v)' = ^{88}Sr (v)/Hz*8. For both types of fluorapatite, $^{87}Sr/^{86}Sr$ ratios in altered domains are systematically higher than those in fresh domains. Note that except for three analyses with much higher $^{87}Sr/^{86}Sr$ ratios, altered domains in vein fluorapatite have a narrower range and lower $^{87}Sr/^{86}Sr$ values than fresh grains.

FIGURE 13. Plot of $\delta^{18}O$ values obtained by *in-situ* SIMS microanalysis and bulk mineral analysis of fluorapatite separates from the Taocun deposit. The altered domains have much lower $\delta^{18}O$ values than the unaltered grains in both disseminated and vein fluorapatite. The insert BSE images show oxygen isotopic variations between unaltered and altered domains in a single fluorapatite grain. Conventional analysis of apatite separates gives values between the altered and unaltered domains, implying a mixed isotopic signature.

FIGURE 14. (**a**) Tera-Wasserburg concordia diagrams of vein fluorapatite from the Taocun deposit. The intercept age was calculated from uncorrected data but was anchored through an initial $^{207}Pb/^{206}Pb$ ratio of = 0.852 ± 0.068 of the intrusion (Xing 1996). (**b**) Weighted mean ^{207}Pb corrected $^{206}Pb/^{238}U$ ages of unaltered vein fluorapatite from the Taocun deposit.

FIGURE 15. Sketches illustrating the formation and metasomatic alteration of the fluorapatite in the Taocun deposit. (**a**) A conceptual model showing the formational environment of disseminated and later-stage, vein-type magnetite ore in the deposit and pathways of metasomatic fluids. (**b**) Enlargement showing the crosscut relationship between disseminated ores and later vein-type magnetite-apatite ores. Multiple sources of the metasomatic fluids are also indicated. (**c**) Sketch showing that disseminated fluorapatite was metasomatically altered by dissolution-reprecipitation processes. The altered grain contains monazite, allanite, and albite inclusions, and both LREE and HREE were significantly remobilized. (**d**) Metasomatized vein fluorapatite has monazite and anhydrite inclusions, but only LREEs are released. Fluorapatite exchanged Sr and O isotopes with the metasomatic fluids, and its trace elements (e.g., REEs, Si, S, Na, Sr, Mg, Fe, V, and Th) were largely leached out.

Always consult and cite the final, published document. See http:/www.minsocam.org or GeoscienceWorld

Fig.1

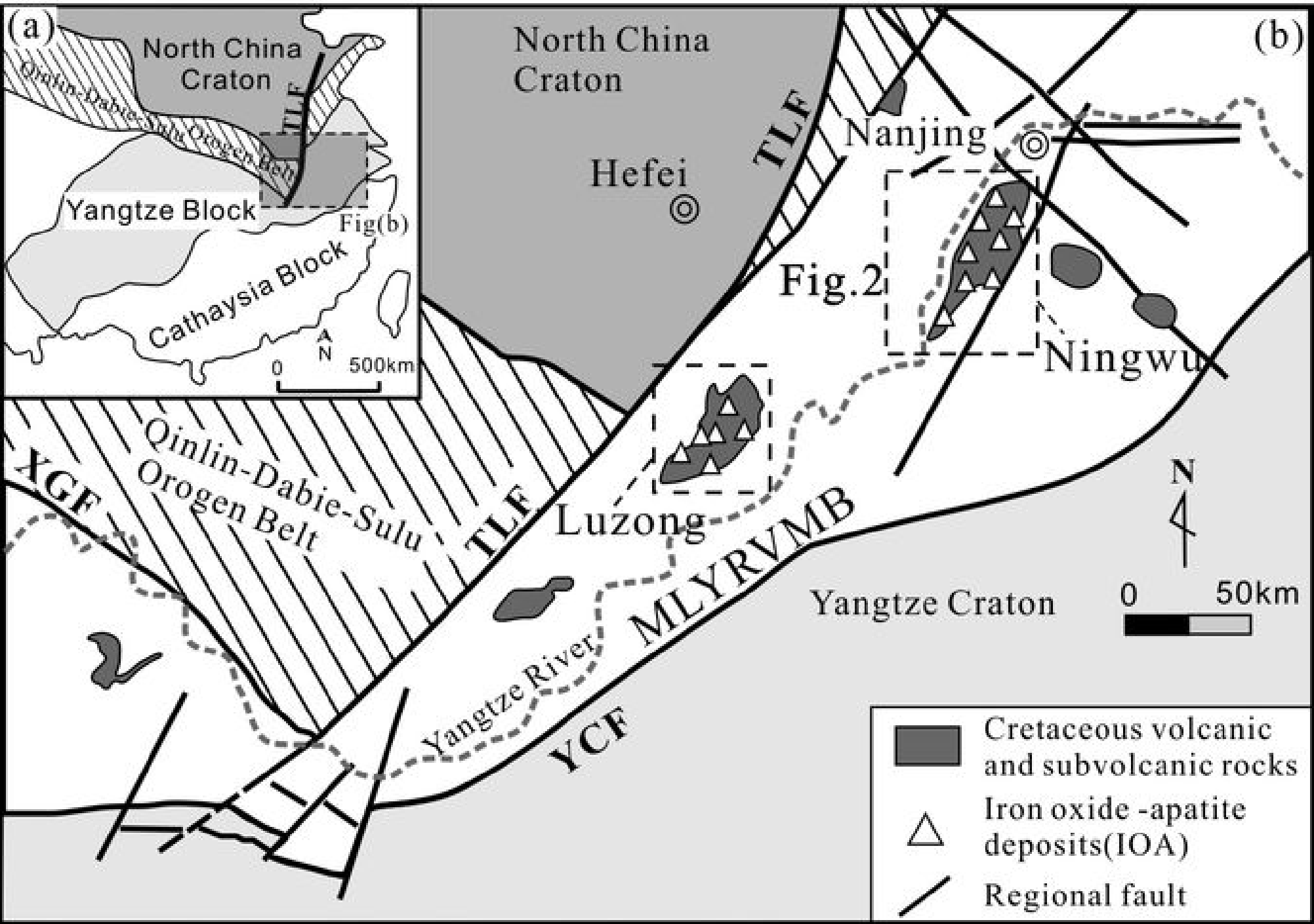
(a)
North China Craton
Qinlin-Dabie-Sulu Orogen Belt
TLF
Yangtze Block
Fig(b)
Cathaysia Block
N
0
500km
North China Craton
TLF
Hefei
Nanjing
(b)
Fig.2
Ningwu
Luzong
XGF
Qinlin-Dabie-Sulu Orogen Belt
TLF
MLYRVMB
Yangtze Craton
N
0
50km
Yangtze River
YCF
Cretaceous volcanic and subvolcanic rocks
Iron oxide -apatite deposits(IOA)
Regional fault

Fig. 2

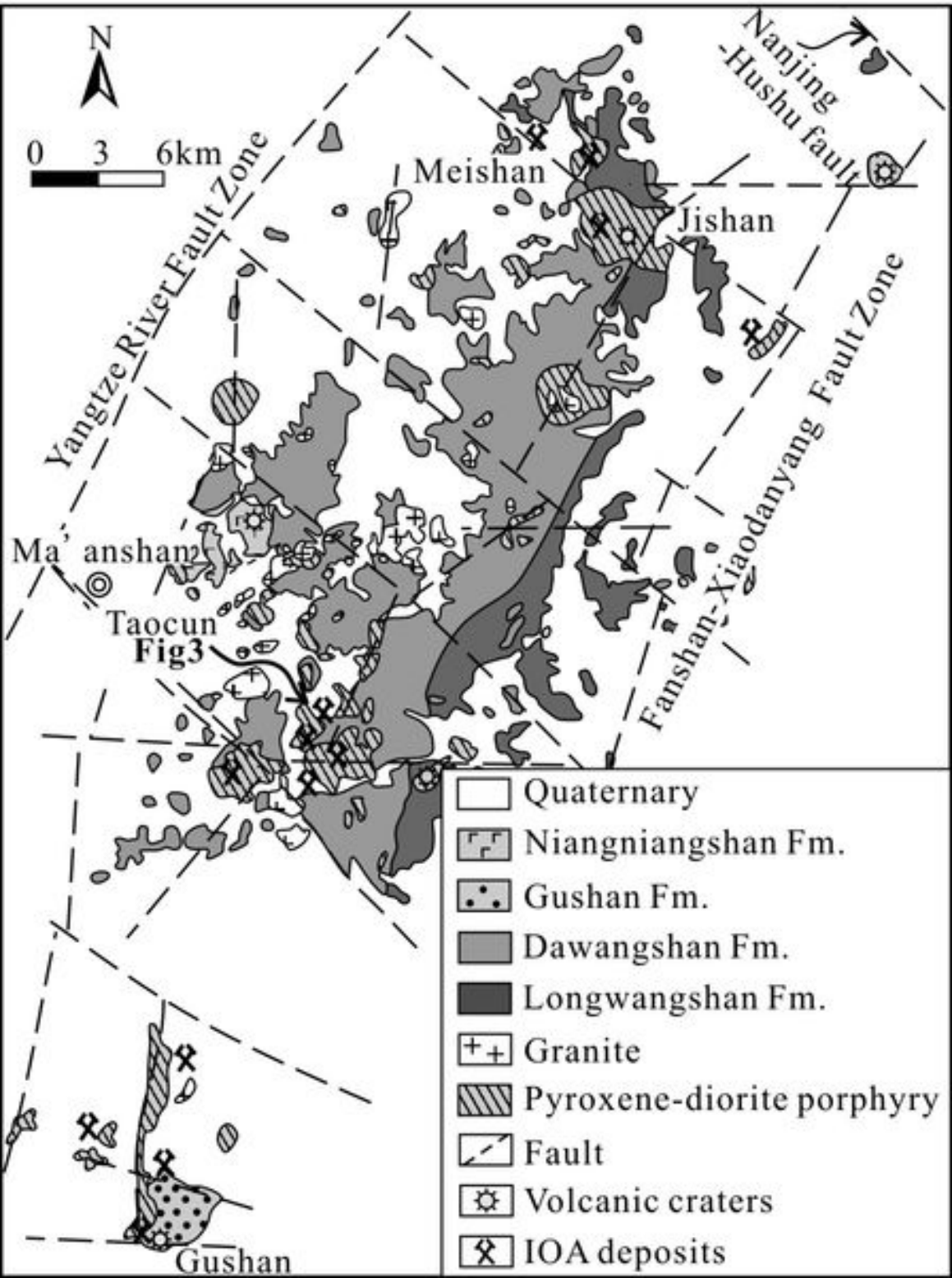
N
0 3 6km
Nanjing
-Hushu fault
Meishan
Jishan
Yangtze River Fault Zone
Fanshan-Xiaodanyang Fault Zone
Ma'anshan
Taocun
Fig3
Gushan
Quaternary
Niangniangshan Fm.
Gushan Fm.
Dawangshan Fm.
Longwangshan Fm.
Granite
Pyroxene-diorite porphyry
Fault
Volcanic craters
IOA deposits

Fig. 3

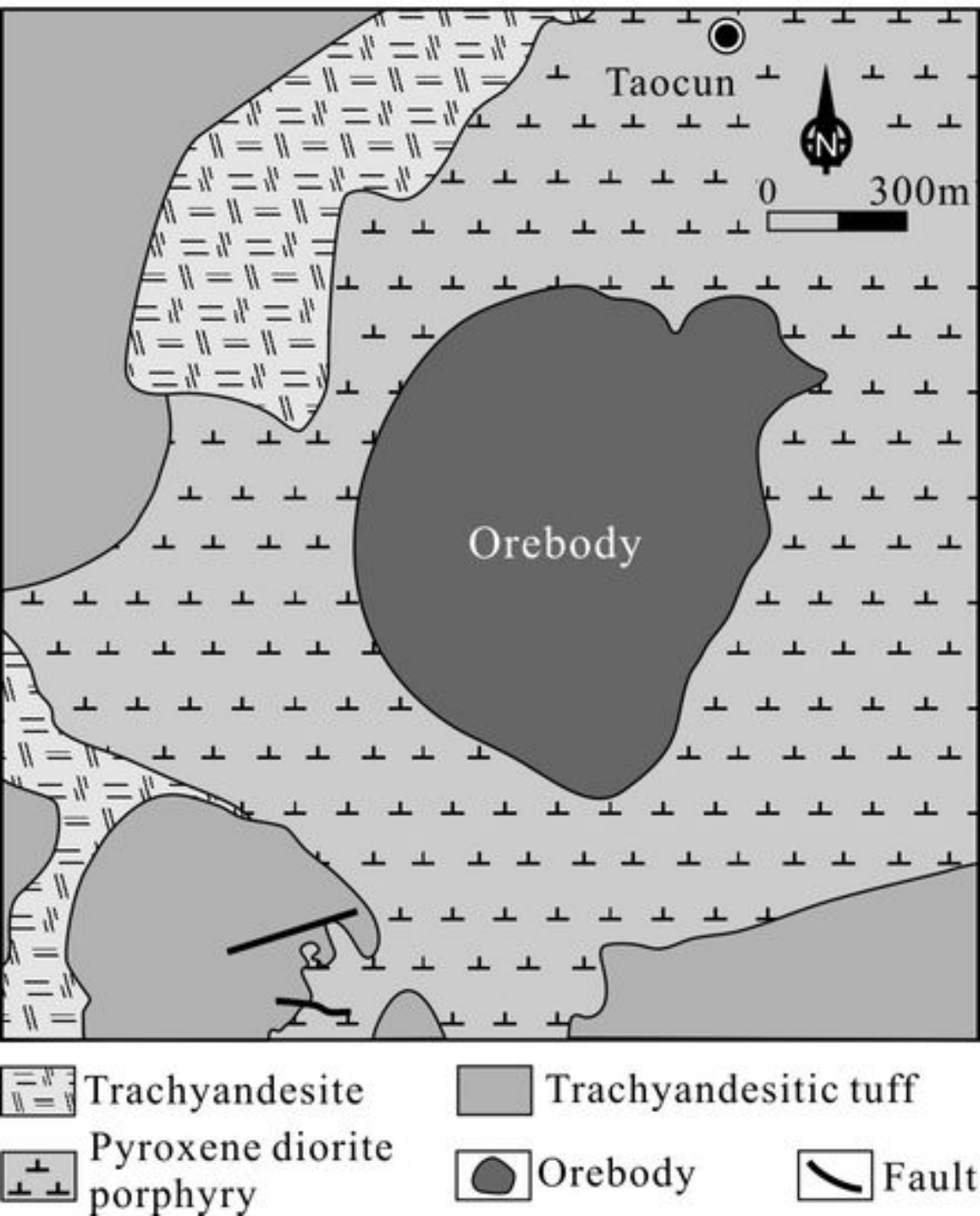
Taocun
N
0
300m
Orebody
Trachyandesite
Trachyandesitic tuff
Pyroxene diorite porphyry
Orebody
Fault

Fig.4

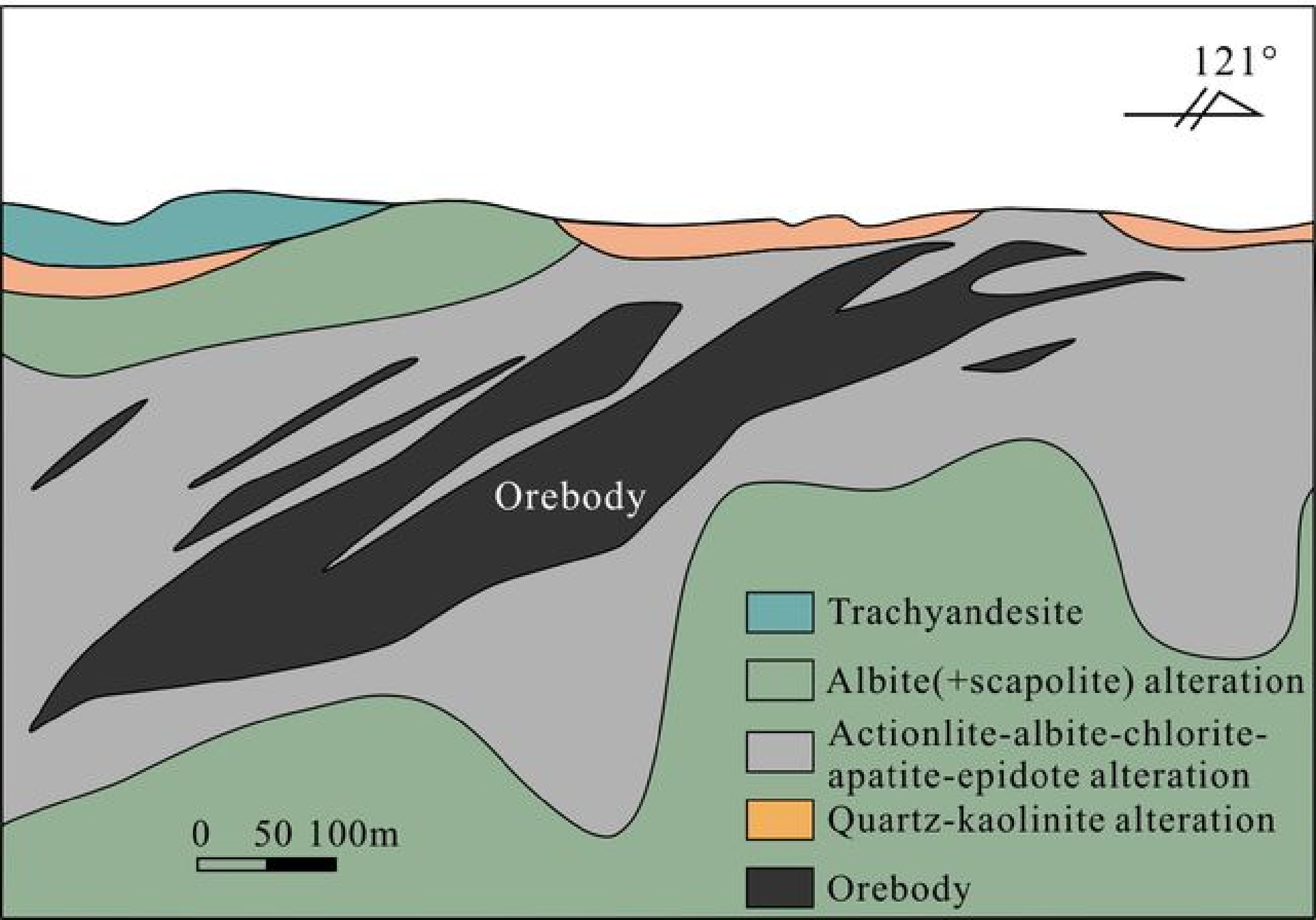
121°
Orebody
0 50 100m
Trachyandesite
Albite(+scapolite) alteration
Actionlite-albite-chlorite-apatite-epidote alteration
Quartz-kaolinite alteration
Orebody

Fig.5

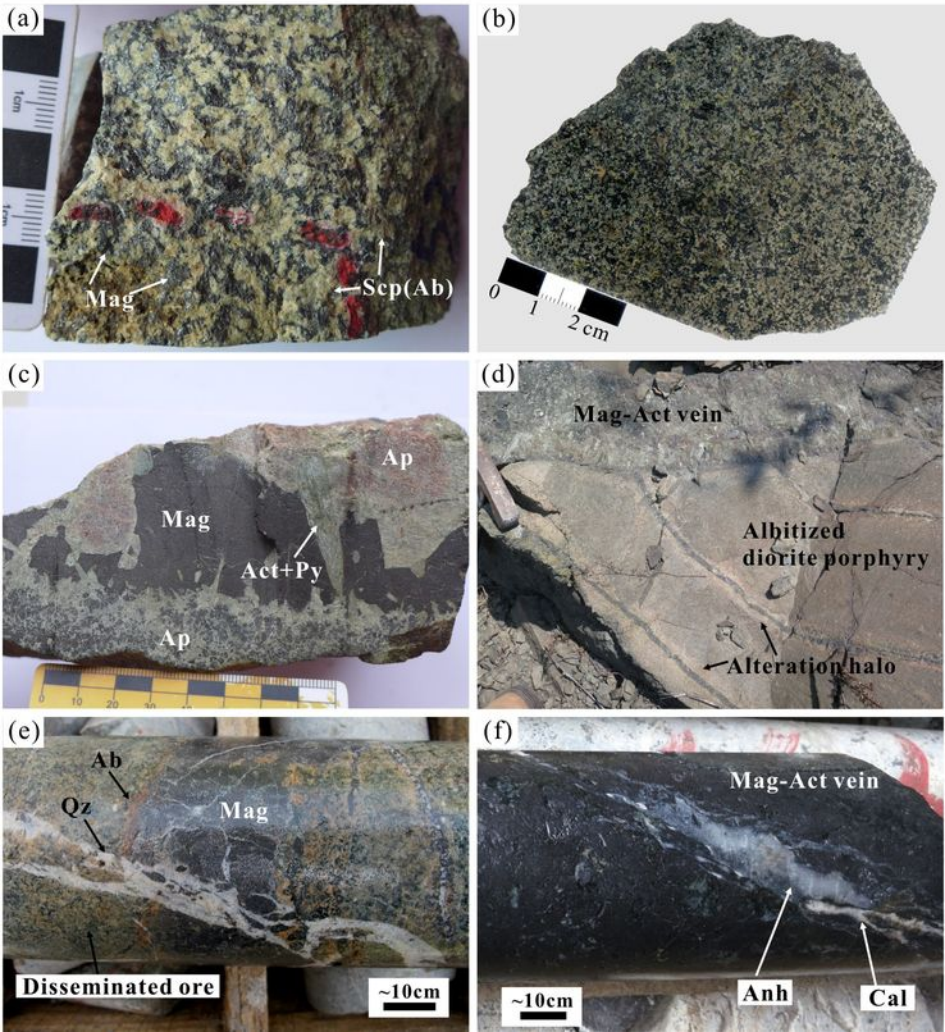
(a)
Mag
Scp(Ab)
(b)
0
1
2 cm
(c)
Ap
Mag
Act+Py
Ap
(d)
Mag-Act vein
Albitized
diorite porphyry
Alteration halo
(e)
Ab
Qz
Mag
Disseminated ore
~10cm
(f)
Mag-Act vein
Anh
Cal
~10cm

Fig. 6

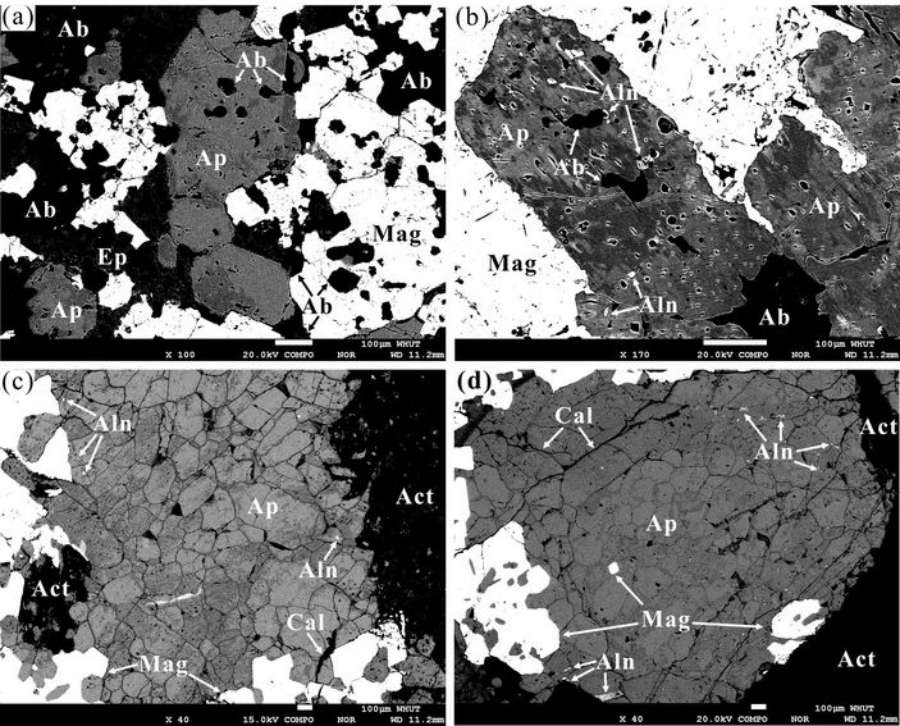
(a)
Ab
Ab
Ab
Ap
Ab
Mag
Ep
Ap
Ab
x 100 20.0kV COMPO NOR WD 11.2mm 100μm MKUT
(b)
Aln
Ap
Ab
Ap
Mag
Aln
Ab
x 170 20.0kV COMPO NOR WD 11.2mm 100μm MKUT
(c)
Aln
Ap
Act
Aln
Act
Cal
Mag
x 40 15.0kV COMPO NOR WD 11.2mm 100μm MKUT
(d)
Cal
Aln
Act
Ap
Mag
Aln
Act
x 40 20.0kV COMPO NOR WD 11.2mm 100μm MKUT

Fig. 7

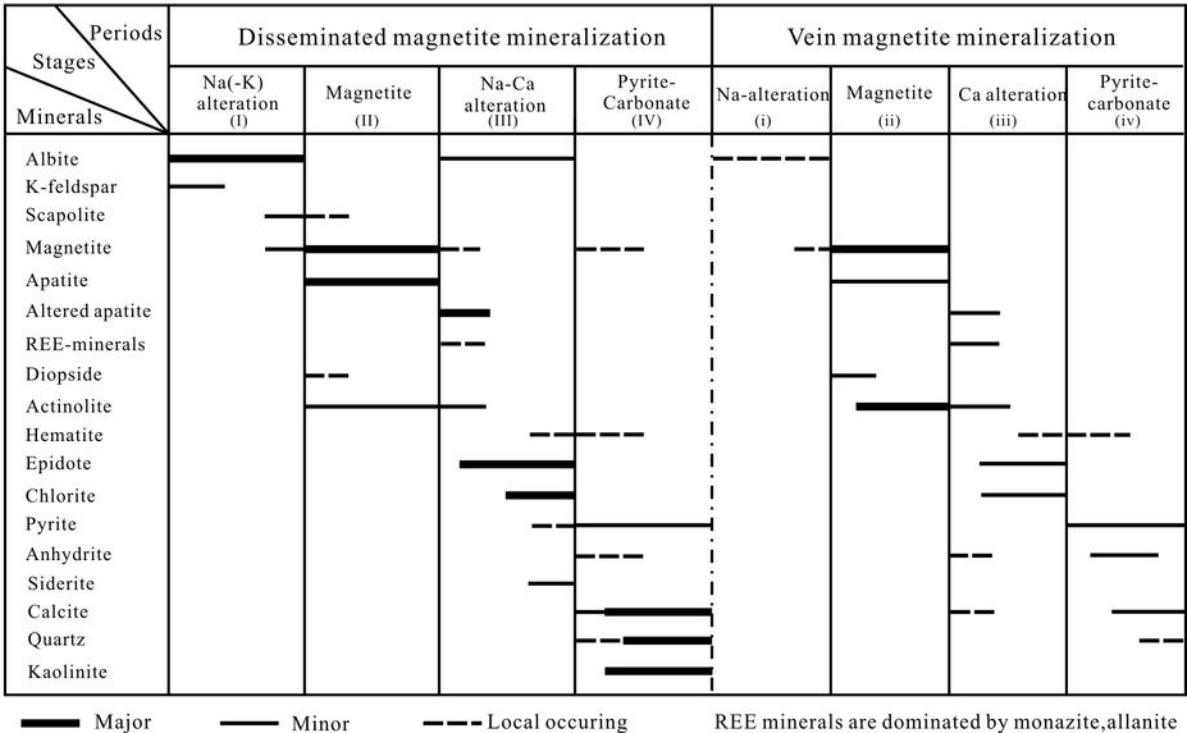
Periods
Stages
Minerals
Disseminated magnetite mineralization
Vein magnetite mineralization
Na(-K) alteration (I)
Magnetite (II)
Na-Ca alteration (III)
Pyrite-Carbonate (IV)
Na-alteration (i)
Magnetite (ii)
Ca alteration (iii)
Pyrite-carbonate (iv)
Albite
K-feldspar
Scapolite
Magnetite
Apatite
Altered apatite
REE-minerals
Diopside
Actinolite
Hematite
Epidote
Chlorite
Pyrite
Anhydrite
Siderite
Calcite
Quartz
Kaolinite
Major
Minor
Local occuring
REE minerals are dominated by monazite,allanite

Fig.8

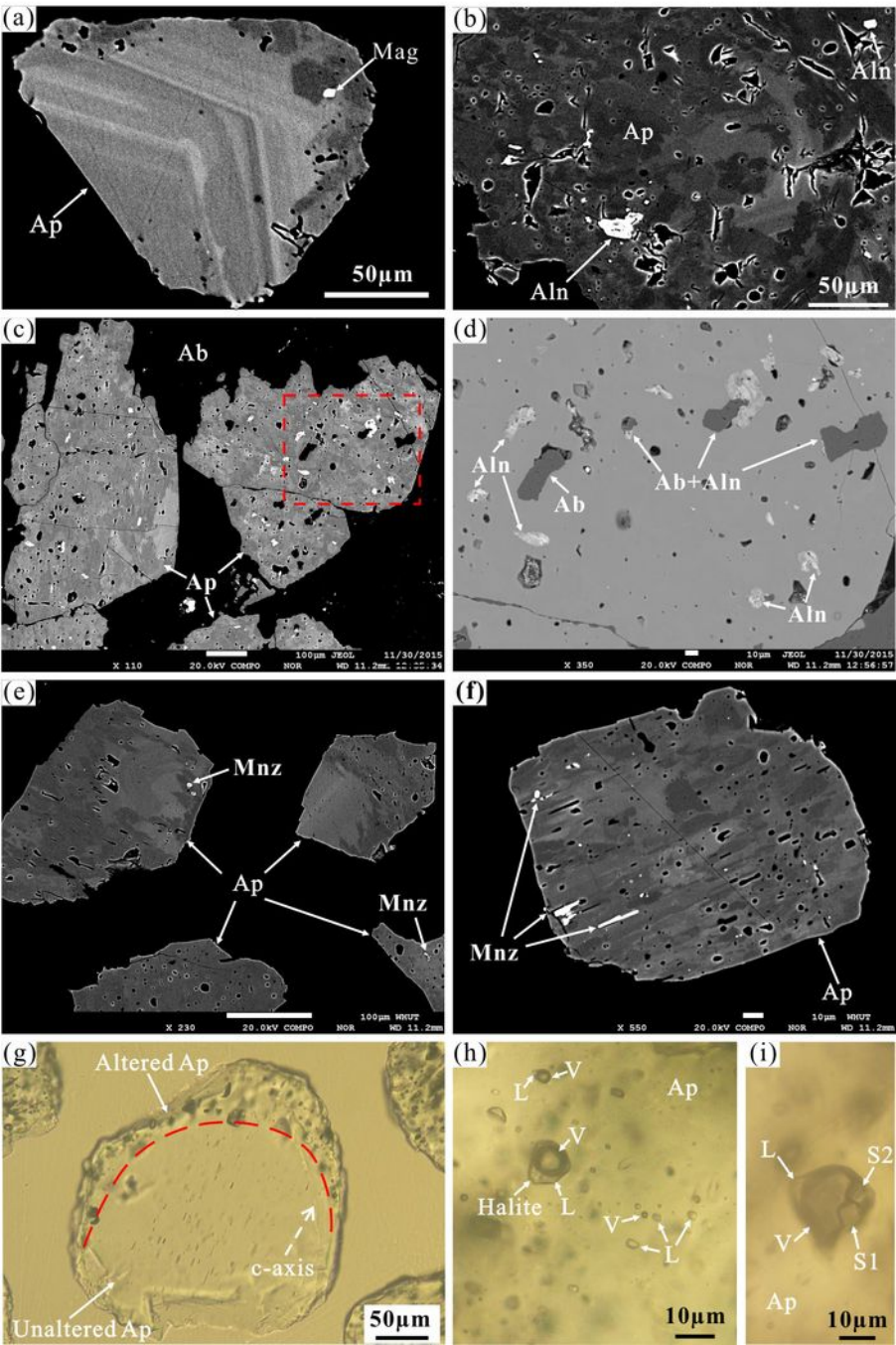
(a)
Mag
Ap
50μm
(b)
Aln
Ap
Aln
50μm
(c)
Ab
Ap
(d)
Aln
Ab
Ab+Aln
Aln
(e)
Mnz
Ap
Mnz
(f)
Mnz
Ap
(g)
Altered Ap
c-axis
Unaltered Ap
50μm
(h)
L
V
Ap
V
Halite
L
V
L
10μm
(i)
L
S2
V
S1
Ap
10μm

Fig.9

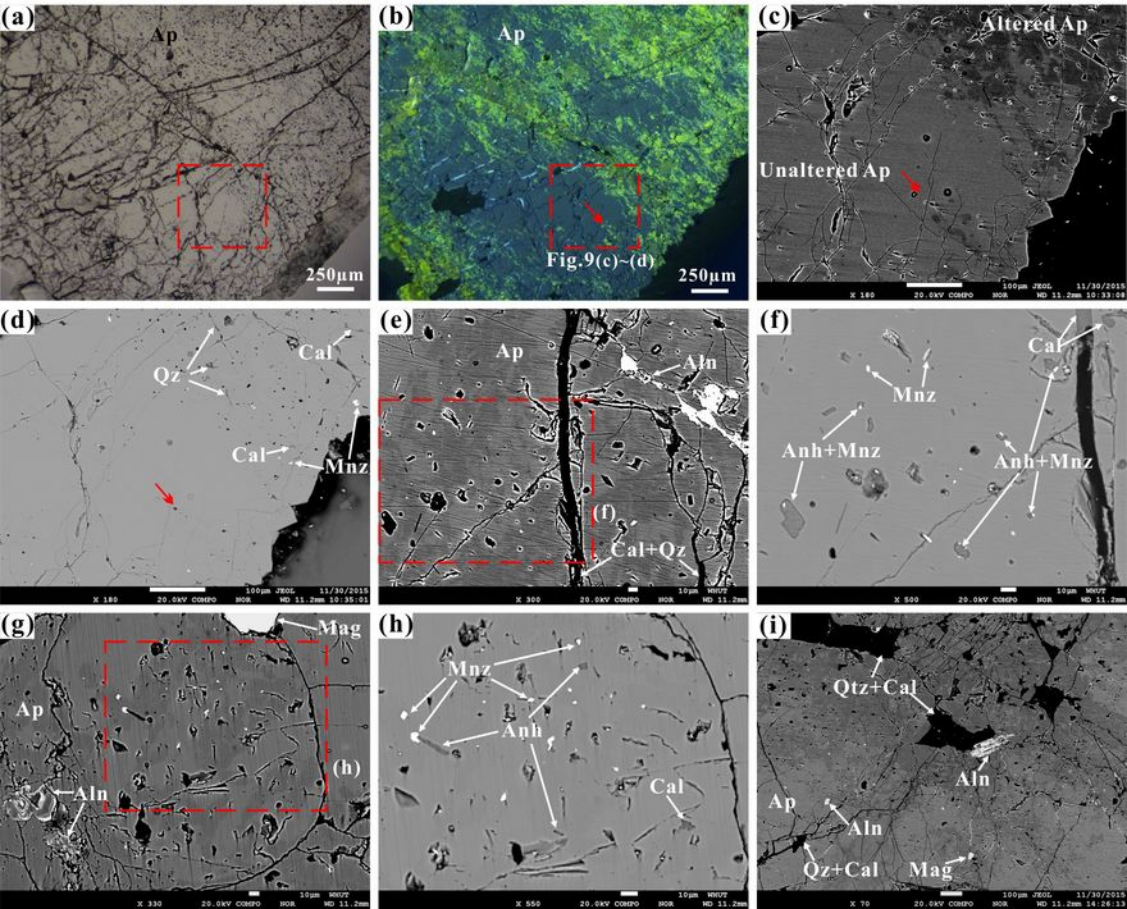
(a)
Ap
250μm
(b)
Ap
Fig.9(c)~(d)
250μm
(c)
Altered Ap
Unaltered Ap
(d)
Qz
Cal
Cal
Mnz
(e)
Ap
Aln
(f)
Cal+Qz
(f)
Cal
Mnz
Anh+Mnz
Anh+Mnz
(g)
Mag
Ap
(h)
Aln
(h)
Mnz
Anh
Cal
(i)
Qtz+Cal
Aln
Ap
Aln
Qz+Cal
Mag

Fig.10

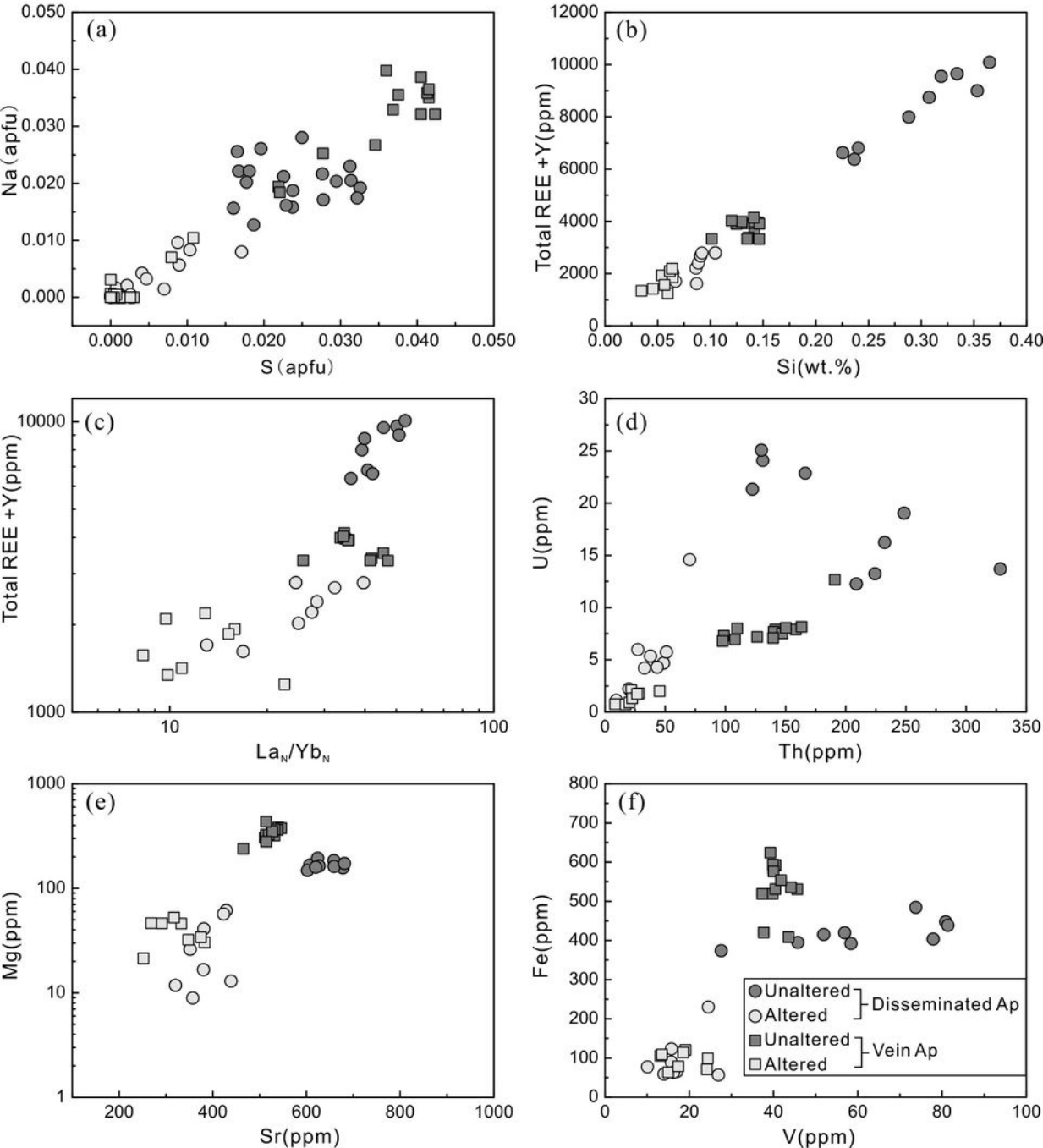
(a)
Na (apfu)
S (apfu)
(b)
Total REE +Y(ppm)
Si(wt.%)
(c)
Total REE +Y(ppm)
La_N/Yb_N
(d)
U(ppm)
Th(ppm)
(e)
Mg(ppm)
Sr(ppm)
(f)
Fe(ppm)
V(ppm)
Unaltered
Altered
Disseminated Ap
Unaltered
Altered
Vein Ap

Fig.11

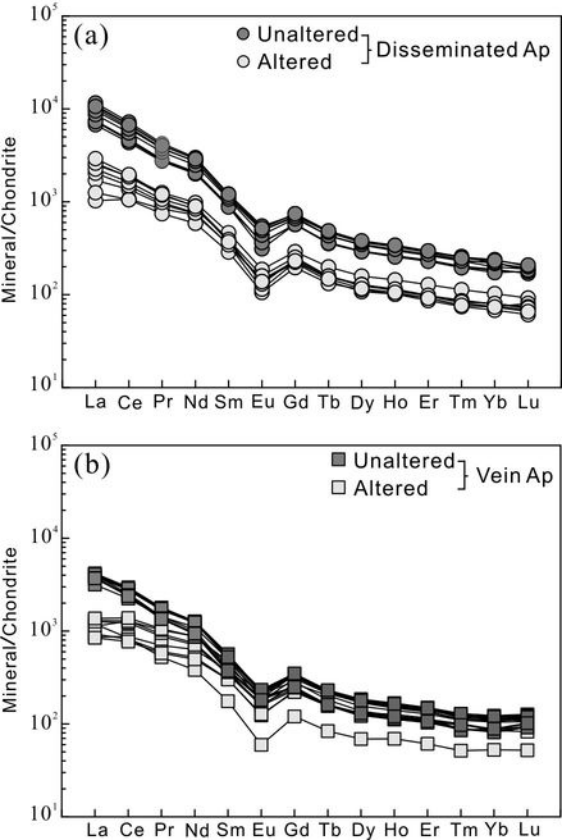
(a)
Unaltered
Altered
Disseminated Ap
Mineral/Chondrite
10^5
10^4
10^3
10^2
10^1
La Ce Pr Nd Sm Eu Gd Tb Dy Ho Er Tm Yb Lu
(b)
Unaltered
Altered
Vein Ap
Mineral/Chondrite
10^5
10^4
10^3
10^2
10^1
La Ce Pr Nd Sm Eu Gd Tb Dy Ho Er Tm Yb Lu

Fig.12

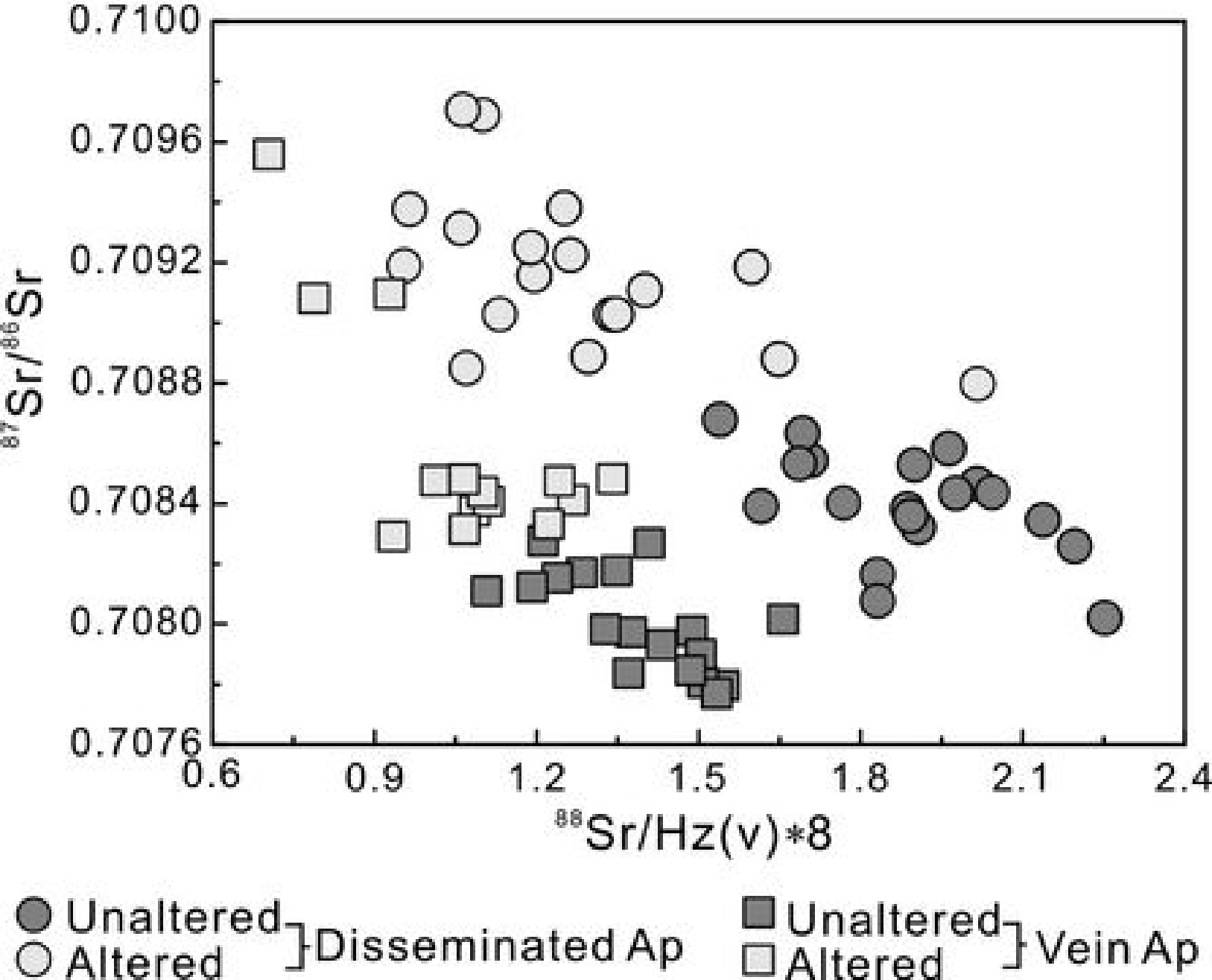
0.7100
0.7096
0.7092
0.7088
0.7084
0.7080
0.7076
$^{87}Sr/^{86}Sr$
0.6
0.9
1.2
1.5
1.8
2.1
2.4
$^{88}Sr/Hz(v)*8$
Unaltered
Altered
Disseminated Ap
Unaltered
Altered
Vein Ap

Fig.13

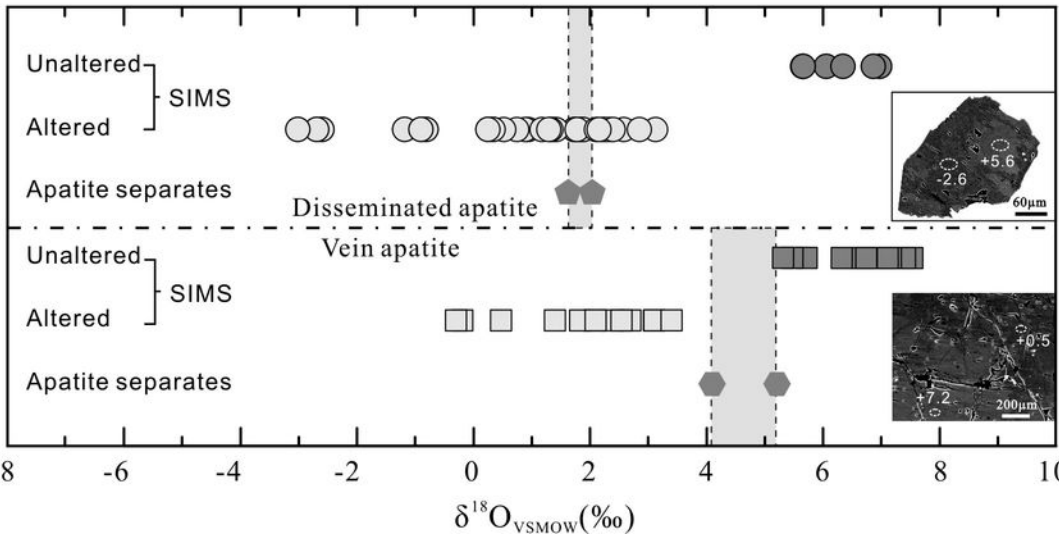
Unaltered
SIMS
Altered
Apatite separates
Disseminated apatite
+5.6
-2.6
60μm
Vein apatite
Unaltered
SIMS
Altered
Apatite separates
+0.5
-7.2
200μm
-8
-6
-4
-2
0
2
4
6
8
10
δ18OVSMOW(‰)

Fig.14

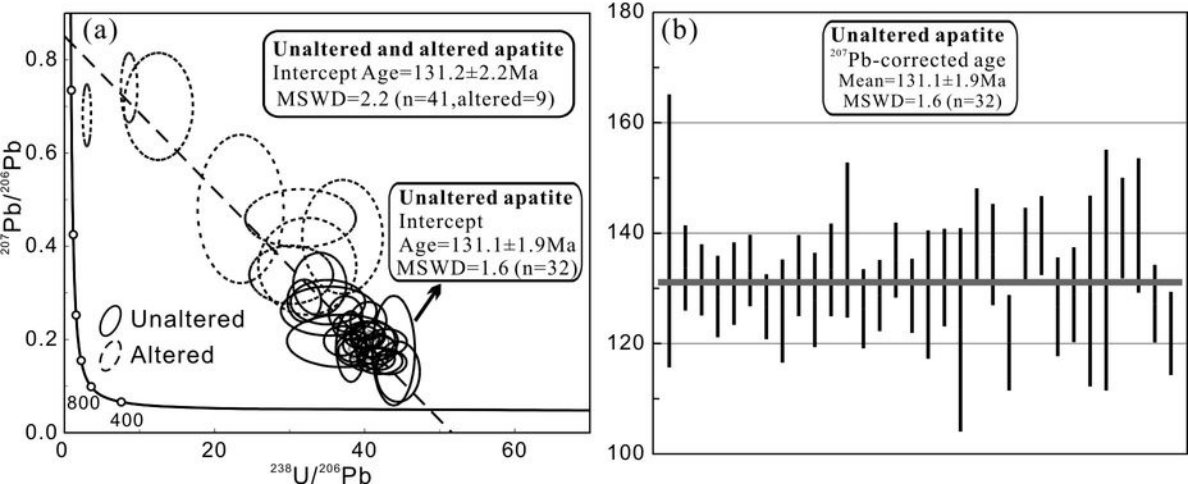
(a)
Unaltered and altered apatite
Intercept Age=131.2±2.2Ma
MSWD=2.2 (n=41,altered=9)
Unaltered apatite
Intercept
Age=131.1±1.9Ma
MSWD=1.6 (n=32)
Unaltered
Altered
800
400
207Pb/206Pb
238U/206Pb
0.0
0.2
0.4
0.6
0.8
0
20
40
60
(b)
Unaltered apatite
207Pb-corrected age
Mean=131.1±1.9Ma
MSWD=1.6 (n=32)
100
120
140
160
180

Fig.15

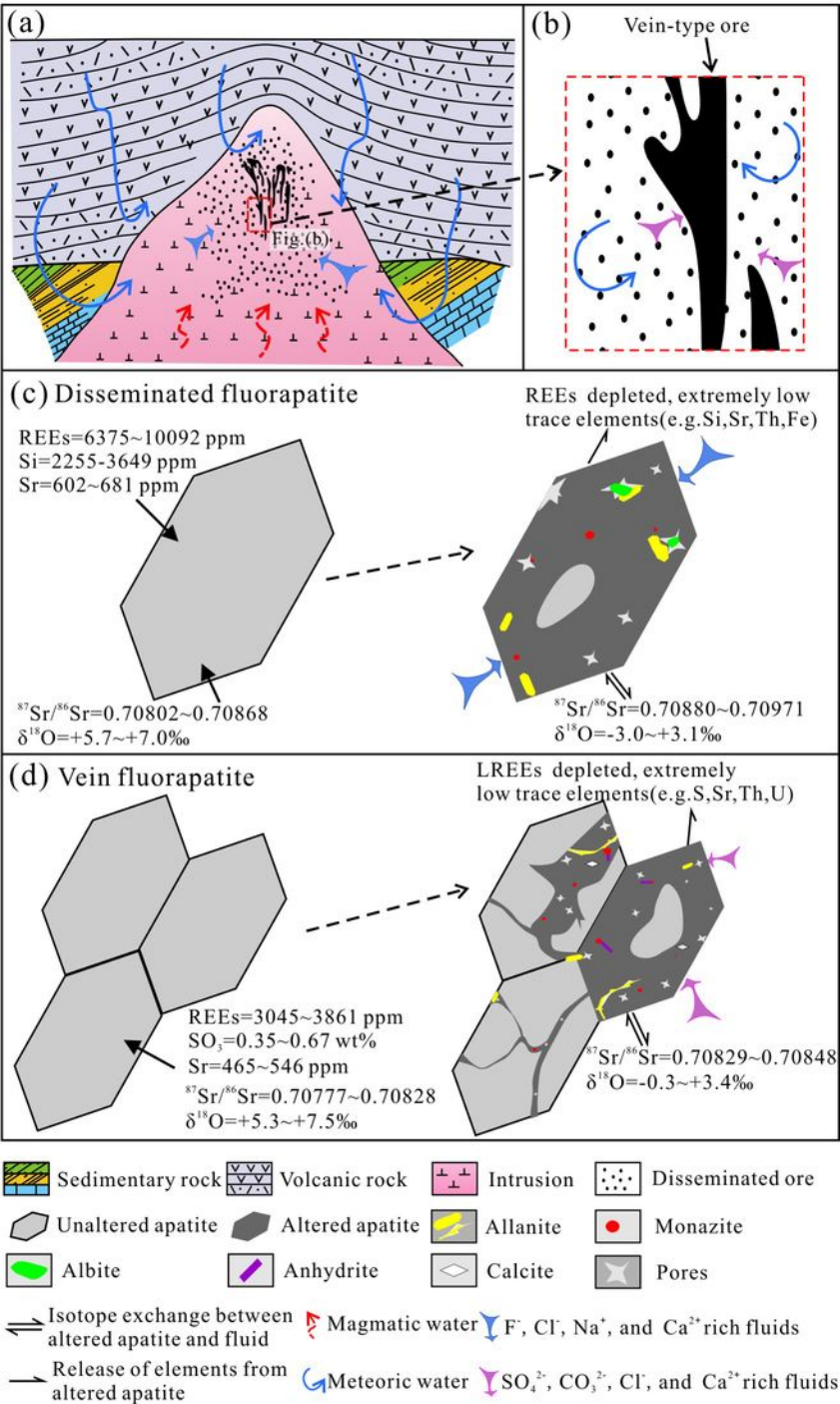
(a)
Fig.(b)
(b)
Vein-type ore
(c) Disseminated fluorapatite
REEs=6375~10092 ppm
Si=2255-3649 ppm
Sr=602~681 ppm
87Sr/86Sr=0.70802~0.70868
δ18O=+5.7~+7.0‰
REEs depleted, extremely low trace elements(e.g.Si,Sr,Th,Fe)
87Sr/86Sr=0.70880~0.70971
δ18O=-3.0~+3.1‰
(d) Vein fluorapatite
REEs=3045~3861 ppm
SO3=0.35~0.67 wt%
Sr=465~546 ppm
87Sr/86Sr=0.70777~0.70828
δ18O=+5.3~+7.5‰
LREEs depleted, extremely low trace elements(e.g.S,Sr,Th,U)
87Sr/86Sr=0.70829~0.70848
δ18O=-0.3~+3.4‰
Sedimentary rock
Volcanic rock
Intrusion
Disseminated ore
Unaltered apatite
Altered apatite
Allanite
Monazite
Albite
Anhydrite
Calcite
Pores
Isotope exchange between altered apatite and fluid
Magmatic water
F-, Cl-, Na+, and Ca2+ rich fluids
Release of elements from altered apatite
Meteoric water
SO4 2-, CO3 2-, Cl-, and Ca2+ rich fluids

Table 1: *In-situ* Sr isotopes of fluorapatite from the Taocun deposit

Sample	$^{85}Rb(v)$	$^{88}Sr(v)$	$Hz(s^{-1})$	$^{88}Sr/Hz*8$	$^{87}Rb/^{86}Sr$	2σ	$(^{87}Sr/^{86}Sr)^{Rb\ cor.}$	2σ
Unaltered domain in disseminated fluorapatite								
NW-99-1	0.00116	1.06684	5	1.70694	0.00358	0.00107	0.70854	0.00077
NW-99-4	0.00066	1.37268	5	2.19629	0.00159	0.00054	0.70826	0.00056
NW-99-5	0.00078	1.25989	5	2.01583	0.00206	0.00058	0.70847	0.00070
NW-99-6	0.00066	1.17949	5	1.88719	0.00184	0.00031	0.70838	0.00069
NW-99-9	0.00046	1.23518	5	1.97628	0.00123	0.00017	0.70843	0.00065
NW-99-10	0.00065	1.14447	5	1.83115	0.00191	0.00077	0.70816	0.00068
NW-99-13	0.00450	1.00954	5	1.61526	0.01496	0.00648	0.70839	0.00080
NW-99-15	0.00106	1.10505	5	1.76808	0.00326	0.00183	0.70840	0.00075
NW-99-16	0.00062	1.27719	5	2.04350	0.00160	0.00060	0.70844	0.00057
NW-99-17	0.00110	0.96235	5	1.53976	0.00377	0.00167	0.70868	0.00089
NW-99-19	0.00112	1.05758	5	1.69212	0.00355	0.00116	0.70863	0.00080
NW-99-20	0.00069	1.33574	5	2.13719	0.00177	0.00095	0.70835	0.00068
NW-99-21	0.00057	1.18728	5	1.89965	0.00163	0.00042	0.70853	0.00079
NW-99-22	0.00041	1.22670	5	1.96272	0.00111	0.00017	0.70858	0.00065
NW-99-25	0.00054	1.19137	5	1.90619	0.00150	0.00046	0.70832	0.00073
NW-99-26	0.00054	1.05389	5	1.68622	0.00169	0.00049	0.70853	0.00086
NW-99-32	0.00049	1.68908	6	2.25211	0.00095	0.00020	0.70802	0.00051
NW-99-35	0.00069	1.41917	6	1.89222	0.00160	0.00076	0.70836	0.00059
NW-99-40	0.00087	1.37357	6	1.83143	0.00206	0.00079	0.70808	0.00059
Altered domain in disseminated fluorapatite								
NW-99-2	0.00141	0.80989	5	1.29582	0.00575	0.00360	0.70889	0.00100
NW-99-3	0.00262	0.68761	5	1.10018	0.01266	0.00989	0.70969	0.00098
NW-99-7	0.00092	1.03021	5	1.64834	0.00299	0.00114	0.70888	0.00078
NW-99-8	0.00099	1.26018	5	2.01629	0.00260	0.00090	0.70880	0.00068
NW-99-11	0.00155	0.83644	5	1.33830	0.00601	0.00620	0.70903	0.00085
NW-99-12	0.00334	0.59676	5	0.95482	0.01886	0.01140	0.70919	0.00094
NW-99-23	0.00396	0.66898	5	1.07037	0.01923	0.00947	0.70885	0.00098
NW-99-24	0.00132	0.74746	5	1.19594	0.00575	0.00263	0.70916	0.00099
NW-99-27	0.00133	0.66290	5	1.06064	0.00660	0.00157	0.70931	0.00097
NW-99-28	0.00057	0.99891	5	1.59825	0.00188	0.00028	0.70919	0.00089
NW-99-30	0.00096	0.78941	5	1.26305	0.00395	0.00250	0.70923	0.00088
NW-99-31	0.00111	0.84857	6	1.13143	0.00431	0.00154	0.70903	0.00095
NW-99-33	0.00090	0.72341	6	0.96454	0.00418	0.00253	0.70938	0.00096
NW-99-34	0.00169	0.89162	6	1.18882	0.00624	0.00304	0.70925	0.00082

NW-99-36	0.00197	0.79764	6	1.06351	0.00817	0.00361	0.70971	0.00089
NW-99-37	0.00193	0.93830	6	1.25107	0.00717	0.00390	0.70938	0.00089
NW-99-38	0.00100	1.05045	6	1.40060	0.00312	0.00108	0.70911	0.00071
NW-99-39	0.00131	1.01099	6	1.34799	0.00427	0.00171	0.70903	0.00079
Unaltered domain in vein fluorapatite								
NW-18-4	0.00051	1.40844	8	1.40844	0.00123	0.00070	0.70827	0.00056
NW-18-5	0.00064	1.34830	8	1.34830	0.00157	0.00069	0.70818	0.00057
NW-18-6	0.00029	1.54736	8	1.54736	0.00062	0.00038	0.70780	0.00048
NW-18-7	0.00053	1.50763	8	1.50763	0.00116	0.00031	0.70781	0.00058
NW-18-8	0.00054	1.53381	8	1.53381	0.00115	0.00033	0.70777	0.00058
NW-18-17	0.00030	1.21238	8	1.21238	0.00086	0.00035	0.70828	0.00060
NW-18-20	0.00033	1.37560	8	1.37560	0.00080	0.00027	0.70797	0.00049
NW-18-21	0.00062	1.28378	8	1.28378	0.00160	0.00080	0.70817	0.00058
NW-18-22	0.00054	1.37031	8	1.37031	0.00134	0.00084	0.70784	0.00056
NW-18-23	0.00046	1.43126	8	1.43126	0.00106	0.00026	0.70793	0.00058
NW-18-2-1	0.00024	1.24220	6	1.65627	0.00062	0.00022	0.70802	0.00067
NW-18-2-2	0.00061	1.11543	6	1.48723	0.00184	0.00043	0.70798	0.00079
NW-18-2-3	0.00052	1.12822	6	1.50429	0.00153	0.00033	0.70790	0.00059
NW-18-2-7	0.00056	0.92889	6	1.23852	0.00200	0.00072	0.70815	0.00088
NW-18-2-8	0.00035	1.11390	6	1.48520	0.00104	0.00028	0.70785	0.00075
NW-18-2-9	0.00037	0.89404	6	1.19206	0.00138	0.00047	0.70812	0.00084
NW-18-2-10	0.00048	0.99559	6	1.32746	0.00162	0.00036	0.70798	0.00087
NW-18-2-11	0.00073	0.83093	6	1.10791	0.00288	0.00102	0.70811	0.00088
Altered domain in vein fluorapatite								
NW-18-2	0.00045	0.70475	8	0.70475	0.00209	0.00049	0.70956	0.00098
NW-18-3	0.00056	0.78776	8	0.78776	0.00238	0.00091	0.70908	0.00095
NW-18-9	0.00155	1.08522	8	1.08522	0.00478	0.00193	0.70838	0.00072
NW-18-10	0.00048	0.92762	8	0.92762	0.00172	0.00051	0.70910	0.00078
NW-18-11	0.00045	1.01408	8	1.01408	0.00147	0.00054	0.70848	0.00071
NW-18-12	0.00075	1.26736	8	1.26736	0.00198	0.00124	0.70841	0.00075
NW-18-13	0.00071	1.22173	8	1.22173	0.00194	0.00102	0.70833	0.00057
NW-18-14	0.00073	1.11091	8	1.11091	0.00217	0.00058	0.70841	0.00070
NW-18-15	0.00050	1.10051	8	1.10051	0.00152	0.00044	0.70844	0.00060
NW-18-16	0.00047	1.06627	8	1.06627	0.00145	0.00045	0.70831	0.00085
NW-18-18	0.00034	1.33984	8	1.33984	0.00083	0.00016	0.70848	0.00055
NW-18-19	0.00024	1.24203	8	1.24203	0.00063	0.00018	0.70848	0.00063

NW-18-2-5	0.00062	0.79900	6	1.06533	0.00250	0.00110	0.70848	0.00082
NW-18-2-12	0.00060	0.70061	6	0.93415	0.00285	0.00196	0.70829	0.00097

Table 2: SIMS oxygen isotopes of fluorapatite from the Taocun deposit

Sample spot#	Sample type	$\delta^{18}O_{VSMOW}$ (‰)	±2σ
In-situ **O isotope in disseminated fluorapattie**			
NW-88@11	Unaltered	6.1	0.3
NW-88@12	Unaltered	5.7	0.3
NW-88@14	Unaltered	6.3	0.3
NW-88@18	Unaltered	7.0	0.3
NW-88@20	Unaltered	6.9	0.3
NW-99@3	Unaltered	5.7	0.3
NW-88@1	Altered	1.7	0.3
NW-88@2	Altered	1.9	0.3
NW-88@3	Altered	1.8	0.3
NW-88@4	Altered	1.7	0.3
NW-88@5	Altered	1.7	0.3
NW-88@6	Altered	1.4	0.3
NW-88@7	Altered	2.3	0.3
NW-88@8	Altered	1.4	0.3
NW-88@9	Altered	2.2	0.3
NW-88@10	Altered	1.8	0.3
NW-88@13	Altered	-2.6	0.3
NW-88@15	Altered	2.3	0.3
NW-88@16	Altered	1.9	0.3
NW-88@17	Altered	-0.8	0.3
NW-88@19	Altered	2.6	0.3
NW-99@1	Altered	0.9	0.3
NW-99@2	Altered	0.9	0.3
NW-99@4	Altered	2.1	0.3
NW-99@5	Altered	-2.7	0.3
NW-99@6	Altered	3.1	0.3
NW-99@7	Altered	-1.2	0.3
NW-99@8	Altered	0.2	0.3
NW-99@9	Altered	0.7	0.3
NW-99@10	Altered	1.2	0.3
NW-99@11	Altered	2.1	0.3
NW-99@13	Altered	2.8	0.3
NW-99@14	Altered	2.4	0.3
NW-99@15	Altered	1.3	0.3

Table 2 (continued)

Sample spot#	Sample type	$\delta^{18}O_{VSMOW}$ (‰)	±2σ
NW-99@16	Altered	0.5	0.3
NW-99@17	Altered	-0.9	0.3
NW-99@18	Altered	1.3	0.2
NW-99@19	Altered	-3.0	0.2
NW-99@20	Altered	0.3	0.2
***In situ* O isotope in vein fluorapattie**			
NW-18@1	Unaltered	5.7	0.2
NW-18@3	Unaltered	7.2	0.2
NW-18@8	Unaltered	6.8	0.2
NW-18@10	Unaltered	7.0	0.2
NW-18@11	Unaltered	5.5	0.2
NW-18@12	Unaltered	7.5	0.2
NW-18@13	Unaltered	7.2	0.2
NW-18@14	Unaltered	7.3	0.2
NW-18@15	Unaltered	7.1	0.2
NW-18@16	Unaltered	5.3	0.2
NW-18@17	Unaltered	6.3	0.2
NW-18@19	Unaltered	7.4	0.2
NW-18@21	Unaltered	6.7	0.2
NW-18@22	Unaltered	7.2	0.2
NW-18@23	Unaltered	6.8	0.2
NW-18@24	Unaltered	7.1	0.2
NW-18@25	Unaltered	6.7	0.2
NW-18@2	Altered	2.7	0.2
NW-18@4	Altered	2.1	0.2
NW-18@5	Altered	2.1	0.2
NW-18@6	Altered	-0.2	0.2
NW-18@7	Altered	3.1	0.2
NW-18@9	Altered	2.4	0.2
NW-18@18	Altered	2.5	0.2
NW-18@20	Altered	3.1	0.2
NW-18@26	Altered	0.5	0.2
NW-18@27	Altered	-0.3	0.2
NW-18@28	Altered	1.8	0.2
NW-18@29	Altered	3.4	0.2

NW-18@30	Altered	1.4	0.2

Table 3: Oxygen isotope compositions of fluorapatite separates from the Taocun deposit

Sample	Sample type	$\delta^{18}O_{VSMOW}$ (‰)	±2σ
NW-88	Disseminated fluorapatite	2.06	0.03
NW-99	Disseminated fluorapatite	1.65	0.02
NW-18	Vein fluorapatite (transparent grains)	5.21	0.02
NW-18	Vein fluorapatite (reddish grains)	4.10	0.03

Table 4: LA-ICPMS U-Pb dating results of vein fluorapatite from the Taocun deposit

Samples	^{232}Th (ppm)	^{238}U (ppm)	Th/U	^{238}U/^{206}Pb	± 2σ%	^{207}Pb/^{206}Pb	± 2σ%	Rho	^{206}Pb/^{238}U Age (Ma)	± 2σ (Ma)	^{206}Pb/^{238}U corr. Age[a] (Ma)	± 2σ (Ma)
Unaltered domain in vein fluorapatite												
NW-32 - 1	225	10.1	22.3	37.0	6.0	0.197	0.046	0.15	171	26	140	25
NW-32 - 3	207	9.7	21.4	40.2	1.9	0.176	0.022	0.17	158	8	134	8
NW-32 - 5	208	10.5	19.9	41.9	1.7	0.158	0.019	0.57	152	6	132	7
NW-32 - 6	170	8.8	19.3	41.0	1.8	0.189	0.024	0.47	155	7	129	8
NW-32 - 7	220	9.8	22.4	37.9	1.7	0.228	0.022	0.12	168	7	131	8
NW-32 - 11	215	10.1	21.3	41.1	1.6	0.162	0.020	0.35	155	6	133	7
NW-32 - 12	217	10.4	20.9	41.3	1.5	0.194	0.019	-0.08	154	6	127	6
NW-32 - 15	133	9.0	14.8	41.2	2.4	0.200	0.031	0.41	155	9	126	10
NW-32 - 16	213	9.8	21.7	40.2	1.8	0.183	0.023	-0.07	159	7	132	8
NW-32 - 17	151	8.6	17.6	40.0	2.2	0.208	0.024	0.27	159	8	128	9
NW-32 - 18	221	9.9	22.3	39.4	1.9	0.191	0.028	0.47	162	8	133	9
NW-32 - 19	213	9.8	21.7	38.2	1.6	0.185	0.062	0.05	167	7	139	14
NW-32 - 20	199	9.6	20.7	40.3	1.8	0.211	0.023	0.10	158	7	126	8
NW-32 - 21	197	10.0	19.6	40.0	1.6	0.204	0.020	0.44	159	6	129	7
NW-32 - 22	197	9.1	21.6	38.9	1.5	0.190	0.022	0.36	164	6	135	7
NW-18 - 1	169	8.8	19.1	43.3	1.9	0.151	0.021	0.06	147	6	129	7
NW-18 - 2	167	8.6	19.4	44.4	2.4	0.131	0.053	0.24	143	8	129	12
NW-18 - 3	147	6.9	21.3	42.0	2.5	0.154	0.023	0.35	151	9	132	9
NW-18 - 5	128	6.2	20.8	43.9	2.3	0.176	0.096	0.03	145	8	122	19
NW-18 - 7	144	7.6	18.8	38.3	1.8	0.178	0.027	0.51	166	8	140	9
NW-18 - 8	116	6.7	17.5	38.9	2.1	0.185	0.027	0.47	164	9	136	9
NW-18 - 9	163	8.2	19.9	40.5	2.0	0.240	0.033	-0.03	157	8	120	9
NW-18 - 10	173	8.2	21.1	39.9	1.5	0.158	0.020	0.20	159	6	138	7
NW-18 - 11	145	8.0	18.1	38.5	1.6	0.176	0.020	0.46	165	7	140	7
NW-18 - 12	162	8.9	18.1	37.5	1.8	0.255	0.031	0.19	170	9	127	10
NW-18 - 13	149	7.7	19.4	41.5	2.2	0.179	0.027	0.20	153	8	129	9
NW-18-3 - 7	122	8.1	15.0	35.1	4.1	0.280	0.039	0.00	181	20	129	18
NW-18-3 - 8	175	7.9	22.2	35.2	5.2	0.261	0.043	0.23	180	26	133	22
NW-18-3 - 9	168	7.9	21.4	36.9	1.9	0.197	0.026	0.37	171	9	141	9
NW-18-3 - 10	169	8.0	21.1	31.9	1.8	0.283	0.037	-0.02	199	11	141	13

Table 4 (continued)

Samples	^{232}Th (ppm)	^{238}U (ppm)	Th/U	$^{238}U/^{206}Pb$	± 2σ%	$^{207}Pb/^{206}Pb$	± 2σ%	Rho	$^{238}U/^{206}Pb$ age	± 2σ Ma	$^{206}Pb/^{238}U$ corr. Age[a] (Ma)	± 2σ Ma
NW-18-3 - 11	185	8.6	21.5	41.8	1.9	0.182	0.021	0.52	152	7	127	7
NW-18-3 - 12	173	8.1	21.4	42.9	2.2	0.194	0.023	0.30	148	7	122	8
Altered domain in vein fluorapatite												
NW-32 - 4	34	0.9	37.8	3.0	0.5	0.681	0.055	-0.12	1720	220	448	208
NW-32 - 13	46	0.8	58.4	12.5	3.8	0.700	0.094	0.85	492	65	97	75
NW-32 - 14	40	1.8	22.9	37.0	4.4	0.420	0.100	0.05	171	20	93	25
NW-18 - 4	63	3	21.5	34.0	2.9	0.319	0.055	0.43	186	16	125	17
NW-18-3 - 1	28	0.9	30.6	23.5	4.7	0.480	0.130	0.71	267	52	126	52
NW-18-3 - 2	29	1.6	19.0	32.4	5.3	0.357	0.085	0.14	196	31	122	29
NW-18-3 - 3	24	1.4	16.9	8.6	0.9	0.740	0.061	0.51	703	70	103	78
NW-18-3 - 4	47	2.7	17.5	30.2	4.6	0.339	0.051	0.45	209	26	135	25
NW-18-3 - 6	84	4.3	19.5	31.4	6.0	0.460	0.051	0.34	202	37	99	24

Note: (a) Common $^{207}Pb/^{206}Pb$ value of 0.852 ± 0.068 (Xing 1996) for a common lead correction.